HHS Public Access

Author manuscript

Cell Rep. Author manuscript; available in PMC 2021 February 17.

Published in final edited form as:

Cell Rep. 2021 February 02; 34(5): 108714. doi:10.1016/j.celrep.2021.108714.

TRPM4 mediates a subthreshold membrane potential oscillation in respiratory chemoreceptor neurons that drives pacemaker firing and breathing

Keyong Li[1], **Stephen B.G. Abbott**[1], **Yingtang Shi**[1], **Pierce Eggan**[1], **Elizabeth C. Gonye**[1], **Douglas A. Bayliss**[1,2,*]

[1]Department of Pharmacology, University of Virginia, Charlottesville, VA 22908, USA

[2]Lead contact

SUMMARY

Brainstem networks that control regular tidal breathing depend on excitatory drive, including from tonically active, CO_2/H^+-sensitive neurons of the retrotrapezoid nucleus (RTN). Here, we examine intrinsic ionic mechanisms underlying the metronomic firing activity characteristic of RTN neurons. In mouse brainstem slices, large-amplitude membrane potential oscillations are evident in synaptically isolated RTN neurons after blocking action potentials. The voltage-dependent oscillations are abolished by sodium replacement; blocking calcium channels (primarily L-type); chelating intracellular Ca^{2+}; and inhibiting TRPM4, a Ca^{2+}-dependent cationic channel. Likewise, oscillation voltage waveform currents are sensitive to calcium and TRPM4 channel blockers. Extracellular acidification and serotonin (5-HT) evoke membrane depolarization that augments TRPM4-dependent oscillatory activity and action potential discharge. Finally, inhibition of TRPM4 channels in the RTN of anesthetized mice reduces central respiratory output. These data implicate TRPM4 in a subthreshold oscillation that supports the pacemaker-like firing of RTN neurons required for basal, CO_2-stimulated, and state-dependent breathing.

In Brief

Li et al. identify a large subthreshold membrane potential oscillation that drives basal and evoked action potential firing in respiratory chemosensory neurons of the mouse RTN. The voltage-dependent oscillation requires L-type calcium channels to activate calcium-dependent TRPM4 cationic channels, inhibition of which suppresses breathing output *in vivo*.

*Correspondence: dab3y@virginia.edu.

AUTHOR CONTRIBUTIONS

K.L., S.B.G.A., and D.A.B. designed experiments, analyzed data, and wrote the manuscript. K.L. and P.E. made *in vitro* electrophysiological recordings, K.L. performed RNAscope *in situ* hybridization histochemistry, and S.B.G.A. performed 9-pt and CBA injections for dEMG recordings in anesthetized mice. Y.S. performed scRNA-seq and E.C.G. helped with data analysis. K.L., S.B.G.A., Y.S., and D.A.B. wrote and/or edited the manuscript.

DECLARATION OF INTERESTS

The authors declare no competing interests.

SUPPLEMENTAL INFORMATION

Supplemental Information can be found online at https://doi.org/10.1016/j.celrep.2021.108714.

Graphical Abstract

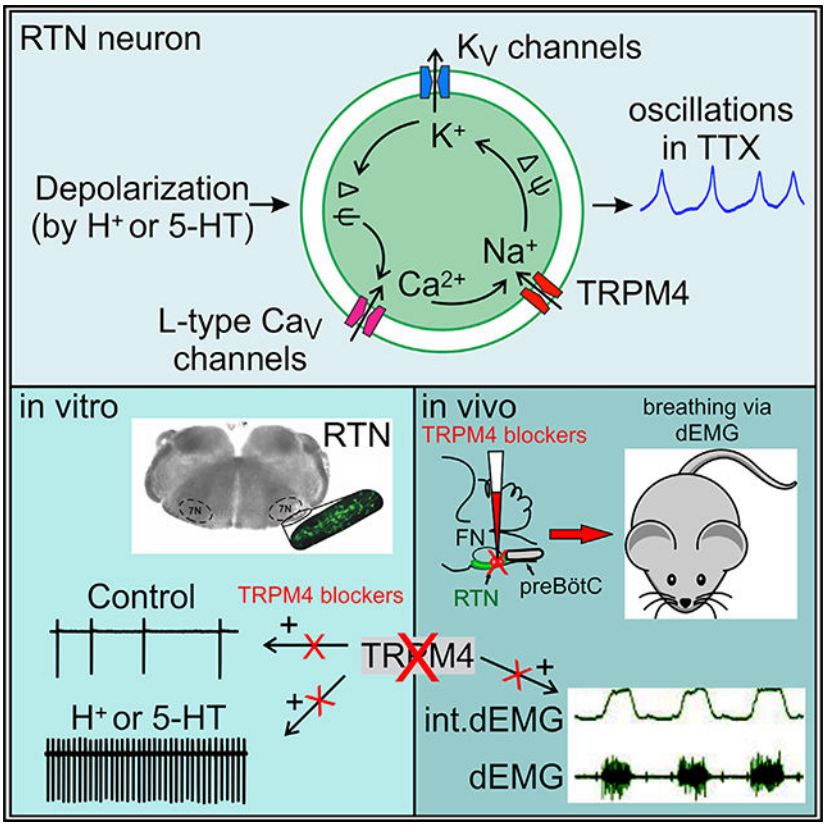

INTRODUCTION

Breathing is an ongoing rhythmic motor activity orchestrated by brainstem networks that regulate its frequency and amplitude; during quiet (i.e., eupneic or tidal) breathing, the activity of brainstem respiratory rhythmogenic networks is maintained by tonic excitatory drive from other brain regions (Del Negro et al., 2018). The chemosensory neurons of the retrotrapezoid nucleus (RTN) are a critical source of excitatory input to those respiratory centers, integrating and relaying CO_2/H^+-dependent tonic activity that is dynamically modulated by various inputs (e.g., respiratory feedback, neurotransmitters, and arousal state) (Guyenet and Bayliss, 2015; Guyenet et al., 2019). The importance of RTN neuron activity for breathing is most evident during non-rapid eye movement (NREM) sleep, when breathing is largely homeostatic and other inputs are dampened (Guyenet and Bayliss, 2015; Guyenet et al., 2019). Indeed, acute optogenetic inhibition of RTN neurons during NREM sleep can transiently eliminate breathing in unanesthetized rodents (Basting et al., 2015; Burke et al., 2015).

RTN neurons fire in a steady pacemaker-like fashion, both *in vivo* and *in vitro*, providing tonic facilitation of respiratory rhythmogenic networks (Guyenet et al., 2005; Mulkey et al., 2004). The mechanisms that account for this regular, ongoing firing activity have not been determined, but the persistence of this firing pattern in brainstem slice preparations after

blocking fast synaptic transmission suggests a role for intrinsic neuronal properties (Guyenet et al., 2005; Mulkey et al., 2004). In different neuronal populations, a variety of intrinsic firing patterns have been identified that depend on an assortment of subthreshold inward currents that promote inter-spike depolarizing potentials. They may include leak (NALCN) and persistent Na^+ currents (tetrodotoxin [TTX]-sensitive or TTX-insensitive; voltage-dependent Na channels [Na_Vs]), hyperpolarization-activated cationic current (I_h; HCN), voltage-activated calcium current (often L-type, Ca_V1, or T-type; Ca_V3), and calcium-dependent cationic currents (I_{CaN}; TRPM4/5); the specific subthreshold voltage trajectories dictated by these channels determine the type of firing pattern observed in different cell types (Bean, 2007; Häusser et al., 2004).

In this study, we used patch clamp recording in mouse brainstem slices to examine ionic mechanisms for the regular spike firing pattern observed in RTN neurons and uncovered a strikingly large subthreshold oscillation mediated by a calcium- and TRPM4-dependent cationic current. These oscillations crowned the membrane depolarization associated with extracellular acidification or neurotransmitter stimulation of RTN neurons. Moreover, pharmacological inhibition of TRPM4 in RTN reduced basal and stimulated neuronal action potential discharge *in vitro* and reduced central respiratory output *in vivo*. Thus, this work defines a distinct active membrane phenomenon mediated by the versatile TRPM4 channel —a large, rhythmic oscillatory membrane potential waveform—which in turn supports the tonic RTN neuronal firing that drives breathing.

RESULTS

A prominent subthreshold oscillation in RTN neurons

Chemosensitive RTN neurons are located ventrolateral to the facial motor nucleus in the brainstem, and among other markers, they universally express Phox2b (Dubreuil et al., 2009; Shi et al., 2017; Stornetta et al., 2006). Phox2b-expressing RTN neurons maintain CO_2/H^+-dependent and highly regular tonic firing activity *in vivo* (Guyenet et al., 2005; Mulkey et al., 2004); this activity provides the brainstem respiratory centers with ongoing excitatory input that is essential for regular rhythmic breathing, especially during NREM sleep (Del Negro et al., 2018; Guyenet and Bayliss, 2015; Guyenet et al., 2019). In brainstem slice preparations from Phox2b::GFP mice (Lazarenko et al., 2009), we recorded a similar tonic firing activity from identified RTN neurons (Figure 1A). Because this tonic firing pattern occurs under conditions in which fast synaptic input is blocked, we considered that it may be dictated by cell-intrinsic, pacemaker-type properties.

To examine subthreshold membrane properties that could contribute to this regular firing behavior, we recorded RTN neurons in brainstem slices under whole-cell current clamp conditions. After blocking spontaneous firing with TTX (0.5 μM; Figure 1A), we found that strong depolarizing current pulses did not evoke action potentials but instead revealed only subthreshold active responses (Figure 1B, arrows). In TTX, we also uncovered a striking membrane potential oscillation in a majority of RTN neurons (87.8%, n = 216/246 cells). The oscillation was voltage dependent, progressing from noisy, small-amplitude membrane potential fluctuations at −50 mV to regular, large amplitude spike-like voltage excursions when the membrane potential was depolarized by direct current (DC) injection (Figures 1C

and 1G–1I). Detailed analysis of the oscillation waveform in a subset of RTN neurons (n = 75) revealed an averaged amplitude of 24 ± 0.8 mV from peak to nadir (Figures 1D–1F; in some cases as large as 45 mV), and phase-plane analysis showed that the depolarizing and hyperpolarizing kinetics of these oscillations (Figure 1D, inset: 0.8 ± 0.04 mV/ms and −1.2 ± 0.09 mV/ms) displayed substantially slower kinetics than those of action potentials in RTN neurons (~50–100 mV/ms; not shown). The oscillations were also analyzed by fast-Fourier transform (FFT) in individual RTN neurons at multiple membrane potentials (n = 19), which revealed that the strongest frequency components were typically in the 2- to 4-Hz band across the voltage range, similar to baseline firing frequencies in RTN neurons (Figures 1G–1I). The oscillations increased in frequency and power at more depolarized potentials (Figures 1G–1I). Compared with action potential firing in the same cells before and after TTX at −40 mV, the subthreshold oscillations consistently occurred at lower frequencies and with longer durations (Figures 1J–1L). The lower frequency may reflect, in part, elimination of TTX-sensitive Na_V current contributions to the initial depolarizing drive potential.

Calcium-dependent TRPM4 channels mediate RTN neuron subthreshold oscillation

We examined the ionic basis for TTX-resistant subthreshold oscillations in RTN neurons by ion substitution and channel pharmacology. The oscillations were retained in the presence of a higher TTX concentration (i.e., 1 μM; n = 4; not shown) and were unaffected by application of TC-N 1752 (10 μM), a pan-Na_V channel blocker (Figures S1A and S1B; Lin et al., 2016). This finding argues that residual actions of unblocked TTX-sensitive or TTX-insensitive Na_Vs are not required for the oscillations. Nevertheless, oscillations were eliminated by substituting $NMDG^+$ for Na^+ in the extracellular solution to block sodium currents more broadly (Figure 2A). In addition, bath addition of 200 μM Cd^{2+}, a non-specific calcium channel blocker, also abolished the membrane oscillations (Figure 2B). A low-voltage-activated Ca^{2+} current carried by T-type calcium channels underlies depolarizing potentials and rhythmic or burst firing in many cell types (Bean, 2007; Häusser et al., 2004; Perez-Reyes, 2003). However, we found that TTA-P2 (1 μM), a broad-spectrum T-type channel inhibitor (Choe et al., 2011), had no effect on the subthreshold oscillations (Figures S1C and S1D). In contrast, the L-type calcium channel blocker nifedipine (10 μM) inhibited the oscillations nearly completely (Figure 2C). The N-type and P/Q-type calcium channel blockers ω-conotoxin MVIIA (CgTx; 1 μM) and ω-agatoxin IVA (AgaTx; 0.2 μM) reduced the oscillations when applied in combination (in either order), albeit less effectively than nifedipine (Figures S1E–S1H). Thus, the oscillations are dependent on non-Na_V sodium channel current and on voltage-activated calcium current that is primarily carried by L-type calcium channels with more modest contributions from N- and P/Q-type channels.

Together, these data suggested the possibility that a channel capable of carrying Ca^{2+}-dependent non-specific cationic current (I_{CaN}) could be involved in the TTX-resistant subthreshold oscillations; those currents are often attributed to TRPM4 or TRPM5 channels (Launay et al., 2002; Prawitt et al., 2003; Wu et al., 2010). Accordingly, and consistent with the intracellular Ca^{2+} dependence of TRPM4/5 channels, we never observed subthreshold oscillations in RTN neurons recorded with 10 mM BAPTA in the pipette (i.e., $[Ca^{2+}]i$ buffered to ~10 nM; n = 0/8). In addition, TTX-resistant subthreshold oscillations were inhibited by flufenamic acid (FFA; 100 μM; Figure 2D), a non-selective compound that

blocks neuronal I_{CaN} and various TRP channels, including TRPM4 and TRPM5 (Wu et al., 2010). To discriminate between those two TRP channels, we exposed cells to 9-phenanthrol (9-pt) or CBA (4-chloro-2-[[2-(2-chlorophenoxy)acetyl]amino]benzoic acid), two compounds that have no effect on TRPM5 and are relatively selective for TRPM4 (Burris et al., 2015; Grand et al., 2008; Guinamard et al., 2014; Ozhathil et al., 2018). As illustrated (Figures 2E and 2F), the membrane potential oscillations were strongly reduced by both 9-pt (30 uM) and CBA (50 μM), consistent with a role for TRPM4.

Trpm4 is expressed in RTN neurons

To examine expression of calcium channel subunits and TRPM4 in RTN neurons, we queried our previously published transcriptomic analysis (Shi et al., 2017; GEO: GSE163155) and performed new histochemical experiments. Based on earlier single-cell RNA sequencing (scRNA-seq) data from RTN neurons (Shi et al., 2017), RTN neurons express transcripts for all specific calcium channel subtypes that were implicated in oscillations (Figure S2A), specifically the L-type channel $Ca_V1.2$ (encoded by *Cacna1c*) and the P- and N-type channels ($Ca_V2.1$, *Cacna1a*; $Ca_V2.2$, *Cacna1b*). Note that transcript expression levels of calcium channel subunits did not quantitatively match their contributions to the subthreshold oscillations. This incongruity is most clearly seen in the case of T-type channels that play essentially no role in the oscillations but are well represented in RTN neurons at the mRNA level (particularly, $Ca_V3.1$, *Cacna1g*; $Ca_V3.2$, *Cacna1h*). These findings may reflect differences in the translation efficiency of these transcripts or proximal localization and preferential coupling of specific Ca_V channel subtypes to TRPM4 channels.

A number of *Trp* channel transcripts were also detected in RTN neurons from the earlier scRNA-seq dataset, and of relevance here (Shi et al., 2017), we found prominent expression of *Trpm4* and very low levels of *Trpm5* (Figure S2B). In this sampling of RTN neurons, ~60% had detectable levels of *Trpm4* transcripts. We also performed multiplex fluorescence *in situ* hybridization to localize *Trpm4* in neurons co-expressing *Neuromedin B* (*Nmb*), a marker that is specific for RTN neurons (Li et al., 2016; Shi et al., 2017). *Trpm4* labeling was observed in *Nmb*-expressing RTN neurons (Figures 2G1 and 2G2) and in other non-RTN cells in the same region (see DAPI nuclei stain, Figure 2G3). Only a few fluorescent puncta were evident in the spinal trigeminal tract (sp5) in these same sections, a sparse background cell labeling expected for a region mostly devoid of cell somata (Figure 2H). We counted the number of *Trpm4*-expressing neurons throughout the rostrocaudal extent of the RTN (i.e., from 6.8 mm to 5.5 mm caudal to bregma; Shi et al., 2017) and found that the distribution closely matched that of Nmb-expressing neurons, with ~62%–95% of Nmb^+ RTN neurons showing detectable levels of *Trpm4* across all levels (Figure 2I; overall 73.8% ± 2.9% $Trpm4^+$;Nmb^+ neurons; n = 5). Similar results were obtained in sections from neonatal mice (Figures S2C and S2D; 77.4% ± 1.9%, n = 4). These data demonstrate expression in RTN neurons of the channels implicated in subthreshold membrane oscillations by our pharmacological experiments.

Oscillation-waveform-evoked calcium and TRPM4 currents in RTN neurons

To determine contributions of calcium and TRPM4 channels during the subthreshold membrane potential oscillation in RTN neurons, we measured currents evoked by an averaged oscillation-waveform command under whole-cell voltage clamp (Figure 3A, top). We recorded oscillation-waveform-evoked currents in the presence of TTX and fast synaptic blockers by using a Cs^+-based, TEA containing pipette solution to eliminate K^+ currents. The currents evoked by the oscillation-waveform include passive leak and capacitive components, in addition to the various ionic currents (Figure 3A, bottom). To eliminate the passive components and uncover contributions from different ion channels of interest, the currents sensitive to specific channel blockers were obtained by digital subtraction.

The oscillation-waveform-evoked current was strongly modulated by Cd^{2+}, which blocks calcium and calcium-dependent currents (Figure 3A, bottom). The digitally subtracted (i.e., Cd^{2+} sensitive) current was transformed according to the oscillation-waveform voltage and plotted as a function of membrane potential (Figure 3B); the Cd^{2+}-sensitive current traced an inward arc throughout the voltage trajectory that reached its maximum inward value just beyond the oscillation-waveform peak and returned to baseline at the nadir of the oscillation-waveform. The peak waveform current was dramatically decreased by Cd^{2+}, whereas the T-type channel blocker TTA-P2 had little effect (Figure 3C). The TRPM4-dependent component of oscillation-waveform current was revealed by using 9-pt (Figure 3D) or CBA (Figure 3E), both of which reduced the peak oscillation-waveform current (Figure 3F). In both cases, the blocker-sensitive inward current became progressively larger through the rising phase and past the peak of the oscillation waveform to reach its maximal amplitude during the repolarizing phase before falling again to a nadir at the most hyperpolarized oscillation-waveform potential (Figures 3D and 3E). The 9-pt-sensitive current was eliminated in the presence of Cd^{2+} (Figure 3G1) and strongly reduced after blocking L-type channels with nifedipine (Figure 3H1), as expected for a calcium-dependent TRPM4 current and consistent with the effects of these calcium channel blockers on membrane oscillations. The residual effect of 9-pt on peak current with the more selective L-type channel block by nifedipine, by comparison to Cd^{2+} (*cf.* Figure 3G2 versus Figure 3H2), likely reflects the minor contributions of N- and P-type calcium channels to the oscillations (see Figures S1E–S1H). We found that the peak oscillation-waveform current was smaller in RTN neurons recorded when BAPTA was substituted for EGTA in the whole-cell pipette (-126.7 ± 19.3 pA, $n = 8$ versus -191.0 ± 8.2 pA, $n = 37$ for BAPTA versus EGTA; $p = 0.0089$, by unpaired t test), further consistent with a component of current dependent on intracellular Ca^{2+}. Moreover, there was essentially no effect of 9-pt on oscillation-waveform current in BAPTA-containing RTN neurons, even as the oscillation-waveform evoked a substantial Cd^{2+}-sensitive calcium current in those same cells (Figure 3I). Thus, a calcium-dependent TRPM4-like inward current is activated by the subthreshold oscillation-waveform in RTN neurons.

K^+ channels, including KCNQ channels, oppose subthreshold oscillations in RTN neurons

We tested contributions of different K^+ currents to TTX-resistant subthreshold oscillations and oscillation-waveform-evoked currents. In a first set of experiments, we applied tetraethylammonium (TEA; 10 mM) to block most delayed rectifier-type voltage-gated K^+

channels as well as BK-type calcium-activated K^+ channels. After application of TEA, the subthreshold oscillations were strongly enhanced (Figure 4A). TEA caused a striking increase in the peak rate of depolarization and the amplitude of the oscillations, particularly in the depolarizing direction (Figure 4B). In addition, TEA increased the oscillation power without affecting oscillation frequency (Figure 4C). We also used additional and more selective pharmacological blockers to examine contributions of specific K^+ channels to the subthreshold oscillations. We did not observe a prominent role for Ca^{2+}-activated K^+ channels in the oscillation because neither a BK channel blocker, paxilline (10 μM), nor an SK channel blocker, apamin (100 nM), had any significant effect on the oscillations (Figure S3). On the other hand, application of ML252 (10 μM) to block KCNQ channels (Cheung et al., 2012; Yu et al., 2010), which are known neuromodulatory targets in RTN neurons (Hawkins et al., 2015; Hawryluk et al., 2012; Mulkey et al., 2007; Wu et al., 2019), increased both the power and the frequency of the subthreshold oscillations (Figures 4D and 4E).

We also examined contributions of TEA- and ML252-sensitive K^+ currents evoked by the oscillation waveform under voltage clamp by using a K^+-based internal solution (Figures 4F–4H). Under these conditions, the net oscillation-waveform-evoked current under control conditions was smaller than that observed with Cs^+-based internal (*cf.* control traces in Figure 3). After either TEA (Figure 4F) or ML252 application (Figure 4G), the oscillation-waveform elicited greater net inward current, which more closely approximated that seen in cells recorded with Cs^+, as expected if TEA and Cs^+ block similar populations of K^+ channels (Figure 4F,G). In addition, the effect on peak current was greater for TEA than for ML252, consistent with its more broad-spectrum K^+ channel inhibition. Nonetheless, the TEA- and ML252-sensitive currents were both outward throughout the oscillation waveform, with the TEA-sensitive current attaining its maximal amplitude just beyond the peak depolarization (Figures 4F and 4G). These data indicate that voltage-dependent K^+ (K_V) currents impede the rising phase of the oscillation and support its repolarization; blocking K_V channels enhances the amplitude of the oscillation, and inhibiting KCNQ channels that are active near resting potentials can also increase oscillation frequency.

TRPM4 channels support spontaneous and pH-dependent firing in RTN neurons

We next tested whether TRPM4-dependent subthreshold oscillations in RTN neurons influence tonic and pH-dependent action potential firing. RTN neurons respond to extracellular acidification with membrane depolarization and increased action potential discharge (Guyenet and Bayliss, 2015; Guyenet et al., 2019; Mulkey et al., 2004). In the RTN, an acid-induced cell-intrinsic depolarization is mediated by inhibition of background K^+ currents, either directly by the H^+-inhibited TASK-2 channel or downstream of the H^+-activated receptor GPR4 (Guyenet and Bayliss, 2015; Guyenet et al., 2019; Kumar et al., 2015; Wang et al., 2013a).

In the presence of TTX, repeated exposures to acidified bath solution (from pH 7.3 to pH 7.0) resulted in a recurring membrane depolarization in RTN neurons that was capped with prominent subthreshold oscillations (Figures 5A, 5C, and 5D). When examined in solutions containing 9-pt, however, pH-sensitive RTN neurons no longer exhibited oscillations during

bath acidification even though the pH-dependent membrane depolarization was completely preserved (Figures 5B, 5E, and 5F). Note also that neither bath acidification (to pH 7.0) nor alkalization (pH 7.5) have any significant effect on subthreshold oscillations when examined under those different pH conditions at the same membrane potential (by injection of DC; Figure S4). Collectively, these data indicate that changes in pH do not directly affect subthreshold oscillations (Figure S4) and inhibition of TRPM4 does not affect the background K^+ channel mechanisms mediating pH-dependent RTN depolarization (Figures 5D and 5F). Instead, blocking TRPM4 eliminates the oscillations that accompany the pH-dependent membrane depolarization (Figures 5C and 5E).

We tested whether inhibition of TRPM4-dependent oscillations would also affect RTN neuron firing responses to extracellular pH changes. For this, we recorded action potential discharge (i.e., in synaptic blockers, but no TTX) in cell-attached mode that minimally disrupts membrane properties and intracellular milieu. As reported previously, bath alkalization (from pH 7.3 to pH 7.5–7.8) resulted in a decrease in firing rate, whereas bath acidification (to pH 7.0) increased firing (Lazarenko et al., 2009; Mulkey et al., 2004; Shi et al., 2016); these effects were well preserved through repeated bouts of alkalization and acidification (Figures 5G and 5I). In contrast, exposure to 9-pt caused a sharp decrease in firing rate at neutral pH and blunted effects on firing rate across the pH range (Figures 5H and 5J). Notably, however, there was no effect of 9-pt on pH sensitivity of firing rate in RTN neurons when normalized to the maximum action potential discharge at pH 7.0 (Figure 5K). Thus, blocking TRPM4 in RTN neurons decreases membrane potential oscillations, excitability, and firing rate, independently of neuronal pH sensitivity.

TRPM4 channel activity supports neuromodulation of RTN neurons

Given the contributions of TRPM4 to subthreshold oscillations and overall RTN neuronal excitability, we tested whether the channel might also have a role in the response to excitatory neuromodulators known to activate RTN neurons. Serotonin (5-HT) is a neurotransmitter derived from brainstem raphe neurons that causes membrane depolarization in part by inhibition of background KCNQ-channel currents that are distinct from the K^+ channels mediating effects of pH changes (Hawkins et al., 2015; Hawryluk et al., 2012; Mulkey et al., 2007; Wu et al., 2019). In cell-attached recordings of action potential firing in RTN neurons, we found that repeated applications of 5-HT increased action potential discharge above baseline when the second application was made in the presence of a vehicle control (DMSO) (Figures 6A and 6B). In contrast, the effect of a second application of 5-HT on firing frequency was markedly diminished when administered in the presence of 9-pt (Figures 6C and 6D). As observed with bath acidification, TTX-resistant subthreshold oscillations induced by depolarizing current in the absence of 5-HT were similar to those observed during the 5-HT-evoked membrane depolarization (Figure 6E). This result suggests that the depolarization itself, rather than some additional effect of 5-HT, is largely responsible for triggering and sustaining the oscillations.

Blocking TRPM4 in the RTN reduces respiratory output *in vivo*

We next tested whether TRPM4 in RTN contributes to breathing in adult mice. We first verified that RTN neurons in adult mice display 9-pt-sensitive, TTX-resistant membrane

potential oscillations *in vitro* (Figures S5A and S5B). We then examined respiratory effects of blocking TRPM4 channels in the RTN. For these experiments, we microinjected 9-pt or CBA into the RTN of freely breathing anesthetized adult Phox2b::GFP mice and measured the frequency and amplitude of diaphragm electromyography (dEMG) activity as an index of central respiratory output. As illustrated for two representative mice, bilateral injections of either 9-pt (Figure 7A) or CBA (Figure 7C), but not vehicle, caused a sustained reduction in respiratory frequency (fR) and a negligible change in dEMG amplitude (dAmp). Poincaré plots of the inter-breath interval following bilateral injections show that TRPM4 blockade increased inter-breath interval (i.e., decreased fR), with little effect on the variability of breathing, as reflected by the spread of the data points (Figures 7B and 7D). Appropriate targeting of drug injections in the RTN was verified post hoc by marking injection sites with red fluorescent latex beads (Figure 7E). Group data were pooled from those cases for which injections were localized within 200 μm of GFP+ cell bodies ventral to the facial nucleus, corresponding to the RTN (Figure 7F). In these cases, bilateral RTN injections of 9-pt (n = 6) and CBA (n = 10) reduced breathing frequency by 36% ± 2% and 35% ± 4%, respectively, with little effect on dAmp, yielding a corresponding decrease of 28% ± 6% and 36% ± 8% in overall respiratory output (fR × dAmp) (Figure 7G). Vehicle injections had no effect on any respiratory variable (Figure 7G). In summary, TRPM4-sensitive oscillations are retained in RTN neurons of adult mice, and inhibition of TRPM4 in the RTN *in vivo* produces a marked reduction in respiratory drive.

DISCUSSION

This work has uncovered a major subthreshold membrane potential oscillation that drives tonic pacemaker-like firing in mouse RTN neurons, a population of cells that serve the respiratory control system as CO_2/H^+ chemosensors and as integrators of peripheral and central afferent input (Del Negro et al., 2018; Guyenet and Bayliss, 2015; Guyenet et al., 2019). The strikingly large oscillations are supported by a I_{CaN} that is carried by TRPM4 and primarily dependent on calcium entry by L-type channels. The voltage-dependent TRPM4-mediated oscillations arise superimposed on the tonic membrane depolarization induced in RTN neurons by extracellular acidification (Mulkey et al., 2004; Wang et al., 2013a) and contribute to firing evoked by acidification and 5-HT, a potent neuromodulator of RTN neurons (Hawkins et al., 2015; Hawryluk et al., 2012; Mulkey et al., 2007; Wu et al., 2019). Consistent with an important role for TRPM4 in the regulation of breathing, microinjection of TRPM4 blockers into the RTN *in vivo* strongly reduced central respiratory drive. Thus, ongoing large-amplitude subthreshold membrane potential oscillations mediated by TRPM4 are required for the steady firing in RTN neurons that maintains rhythmic breathing, a role that is particularly important during quiet waking and NREM sleep (Del Negro et al., 2018; Guyenet and Bayliss, 2015; Guyenet et al., 2019).

TRPM4 and other channels underlying membrane potential oscillations in RTN

Our data implicate voltage-dependent calcium (Ca_V) channels and TRPM4 in large amplitude Ca^{2+}- and Na^+-dependent membrane potential oscillations in RTN neurons. Although both TRPM4 and TRPM5 can mediate an I_{CaN} in other cell types (Launay et al., 2002; Prawitt et al., 2003; Wu et al., 2010), *Trpm5* transcripts are undetectable in the

majority of RTN neurons, whereas *Trpm4* expression is readily detectable in ~60%–80% of those cells. Moreover, the oscillations and oscillatory-waveform-induced inward currents were inhibited by 9-pt and CBA, which are two compounds that inhibit TRPM4 selectively over TRPM5 (Burris et al., 2015; Grand et al., 2008; Guinamard et al., 2014; Ozhathil et al., 2018). Interestingly, although multiple Ca_V channel α subunits are expressed in RTN neurons, our pharmacological exploration indicated that the oscillations depend primarily on L-type channels, with minor roles for N-type and P/Q-type channels. Our observation that oscillation-waveform-evoked TRPM4 currents were preserved in cells recorded with EGTA but eliminated with BAPTA (a faster calcium chelator) suggest that this preferential coupling may reflect a more proximate intracellular localization of L-type channels with TRPM4 (Wang and Augustine, 2015).

The ionic bases for the overall trajectory of the subthreshold membrane potential oscillations remain incompletely characterized in RTN neurons (and other neurons). For example, the contributions of inward currents beyond those carried by L-type Ca channels and TRPM4 channels have not been determined. In earlier work, we found that NALCN constitutes a leak Na^+ channel in RTN neurons (Shi et al., 2016), and the slower oscillation frequency we observed relative to action potential frequency suggests a possible role for TTX-sensitive persistent Na_V currents. Thus, we suspect that these Na^+ currents may provide a depolarizing bias toward the potentials that support the oscillations. With regard to outward currents, we found little role for Ca^{2+}-activated K^+ currents (neither BK nor SK) but showed that TEA-sensitive K_V currents modulate the depolarizing and hyperpolarizing trajectories of the oscillation waveform. Of particular note, we showed that KCNQ channels provide a brake against the subthreshold inward currents, consistent with the prominent role for KCNQ channel inhibition in the activation of RTN neurons by various neurotransmitters (Hawryluk et al., 2012; Sobrinho et al., 2016).

TRPM4 membrane potential oscillations in RTN and control of breathing

Inhibition of TRPM4 in the RTN region of anesthetized mice reduced breathing drive (i.e., dEMG activity). As expected, given the location of the RTN upstream of respiratory rhythm-generating circuits of the preBötzinger complex (preBötC; Del Negro et al., 2018; Guyenet and Bayliss, 2015; Guyenet et al., 2019), injections of 9-pt or CBA into the RTN prominently reduced dEMG burst frequency. This acute inhibition suggests that TRPM4 activity contributes to ongoing tonic RTN neuron firing at prevailing levels of both CO_2/H^+ and neuromodulator tone *in vivo*.

Some points merit discussion regarding the role of TRPM4 in respiratory control. First, breathing disturbances have not been reported in mice with global genetic deletion of TRPM4, although those mice were not examined specifically for respiratory phenotypes (e.g., Demion et al., 2014; Dutta Banik et al., 2018; Simard et al., 2013). With genetic knockouts, there is always the possibility of upregulation and/or functional compensation by other TRP channels in RTN neurons (e.g., TRPC3 and TRPM5; see Figure S2) that could mediate a molecularly distinct I_{CaN} in RTN and/or other respiratory neurons (e.g., preBötC) (Picardo et al., 2019). Even so, a major breathing deficit would not be expected from chronic elimination of TRPM4 from RTN neurons. For example, breathing is well maintained under

baseline conditions by compensatory mechanisms (e.g., by input from peripheral chemoreceptors) even after essentially complete genetic or neurotoxin ablation of RTN neurons (Ramanantsoa et al., 2011; Souza et al., 2018). Second, TRPM4 has previously been associated with respiratory rhythm generation within preBötC neurons, where it was proposed to underlie an I_{CaN} that converts glutamate-receptor-mediated calcium influx into a depolarizing respiratory burst potential (Crowder et al., 2007; Pace et al., 2007; Peña et al., 2004); like the RTN, *Trpm4* is highly expressed in preBötC neurons, whereas *Trpm5* is also undetectable (Hayes et al., 2017). However, more recent pharmacological and gene knockdown studies suggest that TRPM4 in preBötC is dispensable for rhythm generation but instead contributes to respiratory burst amplitude (Koizumi et al., 2018; Picardo et al., 2019). In the current experiments, TRPM4 inhibition in RTN had the opposite effect, primarily inhibiting fR rather than amplitude, suggesting that injected TRPM4 blockers were unlikely to have acted on the nearby preBötC. Together with those earlier results, our findings suggest that TRPM4 plays multiple roles in respiratory rhythm and burst generation by (1) contributing to RTN neuron firing upstream of preBötC to affect fR, as we found here; and (2) modulating burst properties at the preBötC (and perhaps at additional downstream respiratory neurons that contribute to burst amplitude) (Koizumi et al., 2018; Picardo et al., 2019).

TRPM4 and large subthreshold oscillations in other neuronal cell groups

Although not currently attributed to TRPM4, the presence of large, spontaneous neuronal membrane potential oscillations with properties reminiscent of those seen here in RTN neurons have previously been observed in select neuronal populations that are also capable of producing regular, pacemaker-like firing—i.e., in suprachiasmatic nucleus (SCN) neurons that comprise the circadian clock (Jackson et al., 2004; Pennartz et al., 2002), dopaminergic neurons of the substantia nigra pars compacta (SNpc) (Chan et al., 2007; Nedergaard et al., 1993; Nedergaard and Greenfield, 1992; Puopolo et al., 2007; Yung et al., 1991), and noradrenergic neurons of the locus coeruleus (Filosa and Putnam, 2003; Sanchez-Padilla et al., 2014). These oscillations are dependent on L-type calcium channels, as we found for RTN neurons. In SNpc neurons, single-cell RT-PCR and gene knockout experiments suggest that the relevant neuronal L-type channel is likely $Ca_V1.3$ (Chan et al., 2007), whereas in LC neurons, it appears that both $Ca_V1.2$ and $Ca_V1.3$ are involved in the subthreshold oscillation (Sanchez-Padilla et al., 2014). Our single-cell transcriptomic analysis suggests that $Ca_V1.2$ is the most likely L-type channel mediating oscillations in RTN neurons. The slow oscillation in SCN and SNpc neurons was reportedly unaffected by inhibitors of T-type, N-type, or P/Q-type calcium channels (Jackson et al., 2004; Pennartz et al., 2002; Puopolo et al., 2007); although T-type channels are also dispensable for oscillations in RTN neurons, we find that N-type or P/Q-type channels make minor contributions.

For SCN, SNpc, and LC neurons, the clear dependence for the oscillation on extracellular Ca^{2+} and L-type calcium channels supports the commonly held view that those dihydropyridine-sensitive channels directly carry the inward current that drives the inter-event depolarization and the rising phase of the oscillatory waveform (Chan et al., 2007; Filosa and Putnam, 2003; Jackson et al., 2004; Puopolo et al., 2007; Sanchez-Padilla et al., 2014; Surmeier, 2007). However, blocking Ca^{2+} current will also interfere with Ca^{2+}-

dependent channels, including TRPM4 and TRPM5 channels. Indeed, we show that the effect of 9-pt on oscillatory-waveform currents is eliminated after blocking calcium currents or chelating intracellular Ca^{2+}. Thus, a role for either TRPM4 or TRPM5 in the overtly similar subthreshold membrane potential oscillations in those other neurons remains a possibility (Chan et al., 2007; Filosa and Putnam, 2003; Jackson et al., 2004; Puopolo et al., 2007; Sanchez-Padilla et al., 2014; Surmeier, 2007). In this respect, it was reported that SNpc dopamine neurons express TRPM4, and their tonic firing is inhibited by FFA and 9-pt, offering intriguing preliminary support for this possibility (at least in SNpc neurons) (Mrejeru et al., 2011).

Diverse membrane effects of TRPM4 channels

As discussed, large membrane oscillations have not previously been attributed to I_{CaN} or TRPM4. Instead, I_{CaN} and TRPM4/5 channels have been implicated in various other membrane phenomena in neurons. These phenomena include NMDA-induced burst firing (Mrejeru et al., 2011; Zhu et al., 2004), afterdepolarizations following intense discharge or even single action potentials (Schiller, 2004; Shpak et al., 2012; Teruyama et al., 2011; Tsuruyama et al., 2013), and tonic firing behavior on plateau potentials induced by receptor stimulation (e.g., Gαq-coupled muscarinic or metabotropic glutamate receptors in cortical, amygdala, and thalamic reticular neurons) (Egorov et al., 2002, 2006; Lei et al., 2014; O'Malley et al., 2020). Outside the CNS, TRPM4 and TRPM5 in taste receptor cells are required for transduction of bitter, sweet, and umami tastes (Dutta Banik et al., 2018); and in sinoatrial nodal cells, TRPM4 is activated by spontaneous calcium release from the sarcoplasmic reticulum to support diastolic depolarization and regulate heart rate (Guinamard et al., 2015). Thus, transformation of a calcium signal into enhanced excitability by I_{CaN} and TRPM4/5 can be exploited to mediate a wide variety of cellular electroresponsive properties. The current work expands that repertoire of TRPM4 channel functions to include membrane oscillations underlying tonic firing.

Physiological implications of TRPM4-mediated oscillations in RTN neurons

RTN neuron activity provides a critical excitatory input to brainstem respiratory-rhythm-generating circuits, especially during homeostatic breathing (Del Negro et al., 2018; Guyenet and Bayliss, 2015; Guyenet et al., 2019). RTN neurons express a leak Na^+ current, carried by NALCN and further activated by substance P, to provide a depolarizing bias to the membrane potential (Shi et al., 2016). Likewise, other modulatory neurotransmitters (e.g., 5-HT, acetylcholine, and orexin) mediate membrane depolarization of RTN neurons by effects on other ion channels (e.g., KCNQ and HCN) (Hawkins et al., 2015; Hawryluk et al., 2012; Lazarenko et al., 2011; Mulkey et al., 2007; Sobrinho et al., 2016; Wu et al., 2019). In addition, changes in local CO_2/H^+ levels depolarize RTN cells by direct receptor (GPR4) and channel (TASK-2) mechanisms (Gestreau et al., 2010; Kumar et al., 2015; Wang et al., 2013a, 2013b) and by indirect glial purinergic paracrine signaling (Gourine et al., 2010; Guyenet and Bayliss, 2015; Guyenet et al., 2019). Our current findings indicate that the voltage-dependent oscillations driven by TRPM4 support tonic basal activity and depolarization-evoked increases in RTN neuronal firing by such modulators. We speculate that the large TRPM4-dependent membrane potential oscillations provide a safety margin that works together with these modulatory membrane depolarization mechanisms to

maintain the requisite pacemaker-like firing required for adequate drive to respiratory centers, ensuring that breathing can persist across myriad physiological conditions.

STAR★METHODS

RESOURCE AVAILABILITY

Lead contact—Further information and requests for resources and reagents should be directed to, and will be fulfilled by the Lead Contact, Douglas A. Bayliss (dab3y@virginia.edu)

Materials availability—This study did not generate new unique reagents.

Data and code availability—The Source Data for all data presented was submitted with the manuscript. The single cell RNA-Seq dataset referenced in this paper has been deposited at NCBI (GEO Accession#GSE163155)

EXPERIMENTAL MODEL AND SUBJECT DETAILS

Experiments were performed on neonatal (P6-P14) or adult mice (> P60) of either sex, following procedures adhering to National Institutes of Health Animal Care and Use Guidelines and approved by the Animal Care and Use Committee of the University of Virginia. Mice were housed in Allentown Caging HEPA ventilated racks and steam-sterilized caging (up to 4 per cage), with crushed corncob bedding and *ad libitum* access to irradiated Teklad diet (7904 or 7912) and reverse osmosis water provided through an Avidity automatic drinking water system. Animals were exposed to 12 h light/dark cycles in a vivarium maintained at 22–24°C and ~40% relative humidity. We used a Phox2b::GFP BAC transgenic mouse line (Jx99) that was developed by the GENSAT project and characterized previously (Lazarenko et al., 2009). A total of 220 mice were used (190 for *in vitro* slice experiments; 30 for *in vivo* studies), and they were randomly assigned for experimental treatments.

METHOD DETAILS

Mouse brainstem slice preparation—Brainstem slices were prepared from neonatal and adult Phox2b::GFP mice, essentially as previously described (Ting et al., 2014; Wang et al., 2013a). Briefly, pups (P6-P14) were anesthetized with ketamine and xylazine (375 mg/kg and 25 mg/kg, i.m.), rapidly decapitated and brainstem slices (300 μm) were cut in ice-cold sucrose-substituted solution, containing (mM): 260 sucrose, 3 KCl, 5 $MgCl_2$, 1 $CaCl_2$, 1.25 NaH_2PO_4, 26 $NaHCO_3$, 10 D-glucose, and 1 kynurenic acid. Slices were incubated for 30 min at 37°C and subsequently at room temperature in normal Ringer's solution containing (mM): 130 NaCl, 3 KCl, 2 $MgCl_2$, 2 $CaCl_2$, 1.25 NaH_2PO_4, 26 $NaHCO_3$, and 10 D-glucose. Both cutting and incubation solutions were bubbled with 95% O_2 and 5% CO_2.

For older mice (> P60), slices were prepared followed a modified protocol (Ting et al., 2014). Briefly, animals were deeply anesthetized (ketamine and xylazine, 375 mg/kg and 25 mg/kg, i.p.) and transcardially perfused with 25–30 mL of ice-cold NMDG aCSF (in mM:

93 NMDG, 2.5 KCl, 1.2 NaH_2PO_4, 30 $NaHCO_3$, 20 HEPES, 25 D-glucose, 5 Na-ascorbate, 2 Thio-urea, 3 Na-pyruvate, 12 N-acetyl-L-cysteine, 10 $MgSO_4$, 0.5 $CaCl_2$, with pH adjusted to 7.3–7.4 with 10N HCl) that was saturated with 5% CO_2/95% O_2. The mice were rapidly decapitated and the heads were submerged in ice-cold NMDG aCSF, bubbled with 5% CO_2/95% O_2. After extraction from the skull, the brainstem was blocked and sliced (150 μm) in the coronal plane with a vibrating microslicer (DSK super microslicer zero 1, Ted Pella, Inc.) while submerged in the same solution. Slices were allowed to recover for ≤ 15 min in NMDG aCSF at 32–34°C before being transferred into HEPES-holding aCSF (in mM: 92 NaCl, 2.5 KCl, 1.2 NaH_2PO_4, 30 $NaHCO_3$, 20 HEPES, 25 D-glucose, 5 Na-ascorbate, 2 Thio-urea, 3 Na-pyruvate, 12 N-acetyl-L-cysteine, 2 $MgSO_4$, 2 $CaCl_2$, bubbled with 5% CO_2/95% O_2 and with pH adjusted to 7.3–7.4 with KOH or HCl as necessary). The slices were held in this solution until use.

***In vitro* electrophysiology—**Electrophysiological recordings were obtained from GFP-labeled neurons in brainstem slices using either cell-attached or whole-cell configurations at room temperature using pClamp, an Axopatch 200B amplifier, and a Digidata 1322A analog-to-digital converter (all from Molecular Devices). During recording, the brainstem slices were placed in a recording chamber mounted on a fluorescence microscope (Zeiss Axioskop FS) in HEPES-based perfusate, containing (mM): 140 NaCl, 3 KCl, 2 $MgCl_2$, 2 $CaCl_2$, 10 HEPES, 10 D-glucose. The pH of the bath solution was adjusted between 7.0 and 7.8 by addition of HCl or NaOH. For cell-attached recordings of firing rate, as well as whole cell recordings of membrane potential oscillations, we used a pipette solution containing (mM): 17.5 KCl, 112.5 K-gluconate, 1.5 NaCl, 5 Na_2phosphocreatine, 1 $MgCl_2$, 10 HEPES, 0.2 EGTA, 3 Mg-ATP, 0.3 GTP-Tris (pH 7.2, with KOH). For voltage clamp recordings of Ca^{2+} or Na^+ currents evoked by oscillatory-waveforms we used a Cs^+-based internal solution containing (mM): 100 $CsCH_3SO_3$, 1 $MgCl_2$, 0.5 $CaCl_2$, 5 Na_2phosphocreatine, 30 TEACl, 10 HEPES, 10 EGTA, 3 Mg-ATP, 0.3 GTP-Tris (pH 7.2, with CsOH). When filled with these solutions, patch electrodes had a DC resistance of 3–6 MΩ; electrode tips were coated with Sylgard 184 (Dow Corning).

In all experiments, a cocktail of blockers was added (10 μM CNQX, 10 μM bicuculline, 30 μM strychnine) to inhibit fast excitatory (glutamate) and inhibitory transmitters (GABA, glycine). For some experiments, we replaced extracellular Na^+ in the bath with equimolar N-methyl D-glucamine ($NMDG^+$) to block Na^+ currents, and used tetrodotoxin (TTX, 0.5–1 μM) to inhibit TTX-sensitive Na_V channels or TC-N1752, a pan-Na_V channel blocker. We added $CdCl_2$ (200 μM) to the bath to block Ca^{2+} currents non-specifically, and we applied nifedipine (10 μM), ω-conotoxin MVIIA (1 μM), ω-agatoxin IVA (200 nM), or TTA-P2 (1 μM) to inhibit L-type, N-type, P/Q-type and T-type calcium currents. TEA (10 mM) was applied to inhibit delayed rectifier K^+ currents. In addition, we used flufenamate (100 μM) as a broad-spectrum TRP channel blocker, and 9-pt (30 μM) or CBA (50 μM) as selective TRPM4 channel inhibitors. Bath application of 5-HT (10 μM) was used to examine its effects on membrane potential and subthreshold oscillations.

The pH sensitivity of individual RTN neurons was assessed by measuring cell-attached firing responses in bath solutions titrated to different pH levels (pH 7.0 to pH 7.8) at a holding potential (Vh) of −60 mV (Perkins, 2006). Action potentials and subthreshold

oscillations were recorded at membrane potentials achieved by DC current injection under whole cell current clamp conditions; subthreshold oscillations (30 s) were analyzed by phase plane plots (Clampfit, Molecular Devices) and by Fast Fourier Transform (FFT, MATLAB). The power spectral density (PSD) was computed with the MATLAB function "periodogram" for each frequency bin (0.03 Hz), and total power calculated from the integrated area of the full power density spectrum. The mean frequency was calculated by MATLAB function "meanfreq." Membrane potential oscillations were captured under current clamp and used as voltage clamp commands to characterize contributions of select currents to the oscillation-waveform trajectory under whole cell voltage clamp.

***In vivo* RTN injections of 9-phenanthrol and diaphragm EMG recordings—** Adult Phox2b::GFP mice (n = 17 males, 28.6 g; n = 13 females, 24.7 g) were anesthetized with ketamine/dexmedetomidine HCl (100 mg/kg and 0.2 mg/kg, i.p.). Core temperature was maintained at 37°C with a servo-controlled heating pad. Additional doses of anesthetic (10% initial dose) were administered during experiments if mice exhibited a withdrawal response to a strong hind-paw pinch. Pure oxygen was administered through a nose-cone throughout the experiment. Central respiratory output was determined by diaphragm electromyography (dEMG) by implanting teflon-coated silver wire in the diaphragm with a 25-gauge needle. Mice were mounted in a stereotaxic apparatus and a craniotomy was performed to expose the surface of the cerebellum above the RTN. Borosilicate capillaries (1.2 mm O.D, 0.64 I.D, tip size ~30 μm) loaded with drug or vehicle were positioned in the RTN, caudal and ventral to the facial nucleus, based on stereotaxic coordinates (1.4 mm lateral to midline, 2.0 mm caudal to lambda, 5.0 mm ventral to the surface of the cerebellum) and antidromic field potentials elicited by stimulating the mandibular branch of the facial nerve. Bilateral microinjections of vehicle (0.003% DMSO in PBS for 9-pt; 0.001% DMSO in PBS for CBA) and drug (9-pt, 30 μM; CBA, 50 μM) were performed sequentially (left side then right side of the brain) with 3–5 minutes between injections, and at least 10 minutes between injections of vehicle and drug. Each injection consisted of 45 nL of solution delivered by pressure injections over 5–15 s. The effects of 9-pt and CBA were tested in separate experiments, and to minimize any possible sequencing effect caused by injecting drug after vehicle injections, 9-pt and CBA were injected in the RTN without prior injection of vehicle in 2 and 4 mice respectively. Injection sites of drug were marked with red fluorescent latex beads (0.001% v/v, Retrobeads, Lumafluor), either by adding the beads to the injectate or by reloading the pipette with beads following drug injections. To determine injection locations, mice were transcardially perfused with PBS followed by 10% formalin at the end of the recordings. After 24–48 hr in formalin, the brainstem was sectioned (30–50 μm), mounted on slides, coverslipped, and examined for native GFP and "retrobead" fluorescence on a AxioImager M2 microscope (Carl Zeiss). Injection sites were mapped on representative sections drawn using Neurolucida software (version 11, MBF Bioscience). Cases in which injections were not located within 200 μm of the RTN were excluded from the analysis (n = 9/30 mice). Analog recordings of dEMG activity were amplified and filtered (gain x1K, bandpass filter, 100–3000 Hz) and acquired with a Micro1401 digitizer in Spike2 software (v. 10.0) (Cambridge Electronic Design). Signals were processed offline to digitally filter EKG (high pass filter, 300 Hz), and to rectify and integrate the dEMG signal (time constant, 0.03 s). Respiratory frequency (fR) was

determined from the rising integrated EMG signal, and dEMG burst amplitude was measured using a peak detection feature of the software, with the product of fR and dEMG amplitude taken as an index of overall inspiratory drive. Breathing frequency preceding injections varied between 100–205 breaths per minute, but were not statistically different between groups (9-pt: 154 ± 16, n = 6, vehicle: 144 ± 10, n = 9, t = 0.5857, df = 13, p = 0.57 by unpaired t test; CBA: 156 ± 9, n = 10, vehicle: 149 ± 7, n = 6, t = 0.5797, df = 14, p = 0.57) and fR values were therefore normalized to pre-injection values for analysis. Absolute values for dEMG burst amplitude are not informative since they can simply reflect variations in electrode placement; thus, dEMG burst amplitude are normalized to pre-injection values for statistical analysis. The significance of changes in breathing parameters following injections of 9-phenanthrol and CBA was determined using an ordinary two-ANOVA and Sidak's multiple comparisons test.

Immunohistochemistry (IHC) was performed in a subset of cases to generate images for publication. IHC was performed on free-floating at room temperature unless otherwise noted. A one in three series of 30um sections were rinsed, then blocked in a 100 mM Tris-buffered solution of 10% horse serum, 0.1% Triton-X, and 150 mM sodium chloride and incubated with primary antibodies for an hour at room temperature and 4°C overnight. Sections were then rinsed and incubated with secondary antibodies for 60 min and rinsed again before mounting on slides. Slides were covered with ProLong Gold with DAPI antifade mounting medium (P36931, Thermo Fisher Scientific). GFP was visualized using chicken anti-GFP (1:1000, Aves Labs, Davis, CA, Cat # GFP-1020, RRID: AB_10000240) and Alexa Fluor 488 AffiniPure Donkey Anti-Chicken (1:500, Jackson Immunoresearch, West Grove, PA, Cat # 703–545-155, RRID:AB_2340375). ChAT was visualized using goat anti-Chat (1:100, Millipore-Sigma, Cat # AB144P, RRID:AB_2079751) and Alexa Fluor 647 AffiniPure Donkey Anti-Goat (1:500, Jackson Immunoresearch, West Grove, PA, Cat # 705–605-147, RRID: AB_2340437). Images were captured on a AxioImager M2 microscope (Carl Zeiss).

Multiplex *in situ* hybridization and immunohistochemistry—Mice were perfused transcardially with 4% PFA/0.1 M PB. Brains were removed, immersed in the same fixative for 16–18 hours at 4°C, cut in the transverse plane (30 μm) and placed in cryoprotectant (30% ethylene glycol, 20% glycerol, 50 mM sodium phosphate buffer, pH 7.4) at −20°C until further processing. Sections were washed in sterile PBS, mounted onto charged slides, and dried overnight. Sections were incubated in hydrogen peroxide (10 min, 24°C), and then in target retrieval solution (5 min, 98–102°C; Advanced Cell Diagnostics, ACD, Hayward, CA), rinsed in sterile water (x 2), dehydrated in 100% EtOH (5 min), and dried before incubation in protease IV (30 min, 40°C). After rinsing in sterile water (x 2), sections were incubated with RNAscope® catalog oligonucleotide probes for *Trpm4* and *Nmb* transcripts (2 h, 40°C), and processed according to manufacturer instructions provided in the Multiplex Fluorescent Reagent Kit v2 (ACD; RRID:SCR_012481). Slides were covered with Prolong Gold with DAPI anti-fade mounting medium (Molecular Probes, Eugene, OR).

Cell counts and analysis—Serial sections (1:3 series) through the rostrocaudal extent of the RTN were mounted on glass slides, and images were acquired using an epifluorescence

microscope (Zeiss AxioImager Z1) equipped with Neurolucida software. Labeled cells were counted and aligned for averaging according to defined anatomical landmarks (Paxinos and Franklin, 2001). No stereological correction factor was applied and therefore actual cell numbers will be ~3 times higher than counted.

QUANTIFICATION AND STATISTICAL ANALYSIS

Results are presented either as mean ± SEM, or in box-and-whiskers format (median divides a box bounded by the 25^{th} and 75^{th} percentile, with whiskers defining the range). All statistical analyses were performed using GraphPad Prism (v. 8); details of specific tests are provided in the text or figure legends. Statistical significance was set at $p < 0.05$.

Source Data—Data represented in all main and supplemental figures are contained in Source Data.

Supplementary Material

Refer to Web version on PubMed Central for supplementary material.

ACKNOWLEDGMENTS

This work was supported by R01 HL148004 (S.B.G.A.), R01 HL108609 (D.A.B.), and F31 HL154660 (E.C.G.) from the NHLBI and a grant from the CCHS Family Foundation (D.A.B.). We thank Dr. Patrice Guyenet for helpful suggestions, Dr. Ruth Stornetta and Daniel Stornetta for technical assistance, Dr. Suna Onengut-Gumuscu for help depositing RNA-seq data, Christopher Bayliss and Shaofang Shu for general laboratory and animal husbandry support, and Bayliss lab members for comments throughout performance of the work. We also thank Dr. Hui Chen, UVA-Biology, for help with developing the FFT analysis software.

REFERENCES

Basting TM, Burke PG, Kanbar R, Viar KE, Stornetta DS, Stornetta RL, and Guyenet PG (2015). Hypoxia silences retrotrapezoid nucleus respiratory chemoreceptors via alkalosis. J. Neurosci. 35, 527–543. [PubMed: 25589748]

Bean BP (2007). The action potential in mammalian central neurons. Nat. Rev. Neurosci. 8, 451–465. [PubMed: 17514198]

Burke PG, Kanbar R, Basting TM, Hodges WM, Viar KE, Stornetta RL, and Guyenet PG (2015). State-dependent control of breathing by the retrotrapezoid nucleus. J. Physiol. 593, 2909–2926. [PubMed: 25820491]

Burris SK, Wang Q, Bulley S, Neeb ZP, and Jaggar JH (2015). 9-Phenanthrol inhibits recombinant and arterial myocyte TMEM16A channels. Br. J. Pharmacol. 172, 2459–2468. [PubMed: 25573456]

Chan CS, Guzman JN, Ilijic E, Mercer JN, Rick C, Tkatch T, Meredith GE, and Surmeier DJ (2007). “Rejuvenation” protects neurons in mouse models of Parkinson’s disease. Nature 447, 1081–1086. [PubMed: 17558391]

Cheung YY, Yu H, Xu K, Zou B, Wu M, McManus OB, Li M, Lindsley CW, and Hopkins CR (2012). Discovery of a series of 2-phenyl-N-(2-(pyrrolidin-1-yl)phenyl)acetamides as novel molecular switches that modulate modes of K(v)7.2 (KCNQ2) channel pharmacology: identification of (S)-2-phenyl-N-(2-(pyrrolidin-1-yl)phenyl)butanamide (ML252) as a potent, brain penetrant K(v)7.2 channel inhibitor. J. Med. Chem. 55, 6975–6979. [PubMed: 22793372]

Choe W, Messinger RB, Leach E, Eckle VS, Obradovic A, Salajegheh R, Jevtovic-Todorovic V, and Todorovic SM (2011). TTA-P2 is a potent and selective blocker of T-type calcium channels in rat sensory neurons and a novel antinociceptive agent. Mol. Pharmacol. 80, 900–910. [PubMed: 21821734]

Crowder EA, Saha MS, Pace RW, Zhang H, Prestwich GD, and Del Negro CA (2007). Phosphatidylinositol 4,5-bisphosphate regulates inspiratory burst activity in the neonatal mouse preBötzinger complex. J. Physiol. 582, 1047–1058. [PubMed: 17599963]

Del Negro CA, Funk GD, and Feldman JL (2018). Breathing matters. Nat. Rev. Neurosci. 19, 351–367. [PubMed: 29740175]

Demion M, Thireau J, Gueffier M, Finan A, Khoueiry Z, Cassan C, Serafini N, Aimond F, Granier M, Pasquié JL, et al. (2014). Trpm4 gene invalidation leads to cardiac hypertrophy and electrophysiological alterations. PLoS One 9, e115256. [PubMed: 25531103]

Dubreuil V, Barhanin J, Goridis C, and Brunet JF (2009). Breathing with phox2b. Philos. Trans. R. Soc. Lond. B Biol. Sci. 364, 2477–2483. [PubMed: 19651649]

Dutta Banik D, Martin LE, Freichel M, Torregrossa AM, and Medler KF (2018). TRPM4 and TRPM5 are both required for normal signaling in taste receptor cells. Proc. Natl. Acad. Sci. USA 115, E772–E781. [PubMed: 29311301]

Egorov AV, Hamam BN, Fransén E, Hasselmo ME, and Alonso AA (2002). Graded persistent activity in entorhinal cortex neurons. Nature 420, 173–178. [PubMed: 12432392]

Egorov AV, Unsicker K, and von Bohlen und Halbach O (2006). Muscarinic control of graded persistent activity in lateral amygdala neurons. Eur. J. Neurosci. 24, 3183–3194. [PubMed: 17156379]

Filosa JA, and Putnam RW (2003). Multiple targets of chemosensitive signaling in locus coeruleus neurons: role of K+ and Ca2+ channels. Am. J. Physiol. Cell Physiol. 284, C145–C155. [PubMed: 12388081]

Gestreau C, Heitzmann D, Thomas J, Dubreuil V, Bandulik S, Reichold M, Bendahhou S, Pierson P, Sterner C, Peyronnet-Roux J, et al. (2010). Task2 potassium channels set central respiratory CO2 and O2 sensitivity. Proc. Natl. Acad. Sci. USA 107, 2325–2330. [PubMed: 20133877]

Gourine AV, Kasymov V, Marina N, Tang F, Figueiredo MF, Lane S, Teschemacher AG, Spyer KM, Deisseroth K, and Kasparov S (2010). Astrocytes control breathing through pH-dependent release of ATP. Science 329, 571–575. [PubMed: 20647426]

Grand T, Demion M, Norez C, Mettey Y, Launay P, Becq F, Bois P, and Guinamard R (2008). 9-Phenanthrol inhibits human TRPM4 but not TRPM5 cationic channels. Br. J. Pharmacol. 153, 1697–1705. [PubMed: 18297105]

Guinamard R, Hof T, and Del Negro CA (2014). The TRPM4 channel inhibitor 9-phenanthrol. Br. J. Pharmacol. 171, 1600–1613. [PubMed: 24433510]

Guinamard R, Bouvagnet P, Hof T, Liu H, Simard C, and Sallé L (2015). TRPM4 in cardiac electrical activity. Cardiovasc. Res. 108, 21–30. [PubMed: 26272755]

Guyenet PG, and Bayliss DA (2015). Neural control of breathing and CO2 homeostasis. Neuron 87, 946–961. [PubMed: 26335642]

Guyenet PG, Mulkey DK, Stornetta RL, and Bayliss DA (2005). Regulation of ventral surface chemoreceptors by the central respiratory pattern generator. J. Neurosci. 25, 8938–8947. [PubMed: 16192384]

Guyenet PG, Stornetta RL, Souza GMPR, Abbott SBG, Shi Y, and Bayliss DA (2019). The retrotrapezoid nucleus: central chemoreceptor and regulator of breathing automaticity. Trends Neurosci. 42, 807–824. [PubMed: 31635852]

Häusser M, Raman IM, Otis T, Smith SL, Nelson A, du Lac S, Loewenstein Y, Mahon S, Pennartz C, Cohen I, and Yarom Y (2004). The beat goes on: spontaneous firing in mammalian neuronal microcircuits. J. Neurosci. 24, 9215–9219. [PubMed: 15496653]

Hawkins VE, Hawryluk JM, Takakura AC, Tzingounis AV, Moreira TS, and Mulkey DK (2015). HCN channels contribute to serotonergic modulation of ventral surface chemosensitive neurons and respiratory activity. J. Neurophysiol. 113, 1195–1205. [PubMed: 25429115]

Hawryluk JM, Moreira TS, Takakura AC, Wenker IC, Tzingounis AV, and Mulkey DK (2012). KCNQ channels determine serotonergic modulation of ventral surface chemoreceptors and respiratory drive. J. Neurosci. 32, 16943–16952. [PubMed: 23175845]

Hayes JA, Kottick A, Picardo MCD, Halleran AD, Smith RD, Smith GD, Saha MS, and Del Negro CA (2017). Transcriptome of neonatal pre-Bötzinger complex neurones in Dbx1 reporter mice. Sci. Rep. 7, 8669. [PubMed: 28819234]

Jackson AC, Yao GL, and Bean BP (2004). Mechanism of spontaneous firing in dorsomedial suprachiasmatic nucleus neurons. J. Neurosci. 24, 7985–7998. [PubMed: 15371499]

Koizumi H, John TT, Chia JX, Tariq MF, Phillips RS, Mosher B, Chen Y, Thompson R, Zhang R, Koshiya N, and Smith JC (2018). Transient receptor potential channels TRPM4 and TRPC3 critically contribute to respiratory motor pattern formation but not rhythmogenesis in rodent brainstem circuits. eNeuro 5, ENEURO.0332–17.2018.

Kumar NN, Velic A, Soliz J, Shi Y, Li K, Wang S, Weaver JL, Sen J, Abbott SB, Lazarenko RM, et al. (2015). PHYSIOLOGY. Regulation of breathing by CO_2 requires the proton-activated receptor GPR4 in retrotrapezoid nucleus neurons. Science 348, 1255–1260. [PubMed: 26068853]

Launay P, Fleig A, Perraud AL, Scharenberg AM, Penner R, and Kinet JP (2002). TRPM4 is a Ca2+-activated nonselective cation channel mediating cell membrane depolarization. Cell 109, 397–407. [PubMed: 12015988]

Lazarenko RM, Milner TA, Depuy SD, Stornetta RL, West GH, Kievits JA, Bayliss DA, and Guyenet PG (2009). Acid sensitivity and ultrastructure of the retrotrapezoid nucleus in Phox2b-EGFP transgenic mice. J. Comp. Neurol. 517, 69–86. [PubMed: 19711410]

Lazarenko RM, Stornetta RL, Bayliss DA, and Guyenet PG (2011). Orexin A activates retrotrapezoid neurons in mice. Respir. Physiol. Neurobiol. 175, 283–287. [PubMed: 21145990]

Lei YT, Thuault SJ, Launay P, Margolskee RF, Kandel ER, and Siegelbaum SA (2014). Differential contribution of TRPM4 and TRPM5 nonselective cation channels to the slow afterdepolarization in mouse prefrontal cortex neurons. Front. Cell. Neurosci. 8, 267. [PubMed: 25237295]

Li P, Janczewski WA, Yackle K, Kam K, Pagliardini S, Krasnow MA, and Feldman JL (2016). The peptidergic control circuit for sighing. Nature 530, 293–297. [PubMed: 26855425]

Lin Z, Santos S, Padilla K, Printzenhoff D, and Castle NA (2016). Biophysical and pharmacological characterization of Nav1.9 voltage dependent sodium channels stably expressed in HEK-293 cells. PLoS One 11, e0161450. [PubMed: 27556810]

Mrejeru A, Wei A, and Ramirez JM (2011). Calcium-activated non-selective cation currents are involved in generation of tonic and bursting activity in dopamine neurons of the substantia nigra pars compacta. J. Physiol. 589, 2497–2514. [PubMed: 21486760]

Mulkey DK, Stornetta RL, Weston MC, Simmons JR, Parker A, Bayliss DA, and Guyenet PG (2004). Respiratory control by ventral surface chemoreceptor neurons in rats. Nat. Neurosci. 7, 1360–1369. [PubMed: 15558061]

Mulkey DK, Rosin DL, West G, Takakura AC, Moreira TS, Bayliss DA, and Guyenet PG (2007). Serotonergic neurons activate chemosensitive retrotrapezoid nucleus neurons by a pH-independent mechanism. J. Neurosci. 27, 14128–14138. [PubMed: 18094252]

Nedergaard S, and Greenfield SA (1992). Sub-populations of pars compacta neurons in the substantia nigra: the significance of qualitatively and quantitatively distinct conductances. Neuroscience 48, 423–437. [PubMed: 1603327]

Nedergaard S, Flatman JA, and Engberg I (1993). Nifedipine- and omega-conotoxin-sensitive Ca2+ conductances in guinea-pig substantia nigra pars compacta neurones. J. Physiol. 466, 727–747. [PubMed: 8410714]

O'Malley JJ, Seibt F, Chin J, and Beierlein M (2020). TRPM4 conductances in thalamic reticular nucleus neurons generate persistent firing during slow oscillations. J. Neurosci. 40, 4813–4823. [PubMed: 32414784]

Ozhathil LC, Delalande C, Bianchi B, Nemeth G, Kappel S, Thomet U, Ross-Kaschitza D, Simonin C, Rubin M, Gertsch J, et al. (2018). Identification of potent and selective small molecule inhibitors of the cation channel TRPM4. Br. J. Pharmacol. 175, 2504–2519. [PubMed: 29579323]

Pace RW, Mackay DD, Feldman JL, and Del Negro CA (2007). Inspiratory bursts in the preBötzinger complex depend on a calcium-activated nonspecific cation current linked to glutamate receptors in neonatal mice. J. Physiol. 582, 113–125. [PubMed: 17446214]

Paxinos G, and Franklin KBJ (2001). The mouse brain in stereotaxic coordinates Compact, 2nd edition (San Diego. CA: Elsevier Press).

Peña F, Parkis MA, Tryba AK, and Ramirez JM (2004). Differential contribution of pacemaker properties to the generation of respiratory rhythms during normoxia and hypoxia. Neuron 43, 105–117. [PubMed: 15233921]

Pennartz CM, de Jeu MT, Bos NP, Schaap J, and Geurtsen AM (2002). Diurnal modulation of pacemaker potentials and calcium current in the mammalian circadian clock. Nature 416, 286–290. [PubMed: 11875398]

Perez-Reyes E (2003). Molecular physiology of low-voltage-activated t-type calcium channels. Physiol. Rev. 83, 117–161. [PubMed: 12506128]

Perkins KL (2006). Cell-attached voltage-clamp and current-clamp recording and stimulation techniques in brain slices. J. Neurosci. Methods 154, 1–18. [PubMed: 16554092]

Picardo MCD, Sugimura YK, Dorst KE, Kallurkar PS, Akins VT, Ma X, Teruyama R, Guinamard R, Kam K, Saha MS, and Del Negro CA (2019). Trpm4 ion channels in pre-Bötzinger complex interneurons are essential for breathing motor pattern but not rhythm. PLoS Biol. 17, e2006094. [PubMed: 30789900]

Prawitt D, Monteilh-Zoller MK, Brixel L, Spangenberg C, Zabel B, Fleig A, and Penner R (2003). TRPM5 is a transient Ca2+-activated cation channel responding to rapid changes in [Ca2+]i. Proc. Natl. Acad. Sci. USA 100, 15166–15171. [PubMed: 14634208]

Puopolo M, Raviola E, and Bean BP (2007). Roles of subthreshold calcium current and sodium current in spontaneous firing of mouse midbrain dopamine neurons. J. Neurosci. 27, 645–656. [PubMed: 17234596]

Ramanantsoa N, Hirsch MR, Thoby-Brisson M, Dubreuil V, Bouvier J, Ruffault PL, Matrot B, Fortin G, Brunet JF, Gallego J, and Goridis C (2011). Breathing without CO(2) chemosensitivity in conditional Phox2b mutants. J. Neurosci. 31, 12880–12888. [PubMed: 21900566]

Sanchez-Padilla J, Guzman JN, Ilijic E, Kondapalli J, Galtieri DJ, Yang B, Schieber S, Oertel W, Wokosin D, Schumacker PT, and Surmeier DJ (2014). Mitochondrial oxidant stress in locus coeruleus is regulated by activity and nitric oxide synthase. Nat. Neurosci. 17, 832–840. [PubMed: 24816140]

Schiller Y (2004). Activation of a calcium-activated cation current during epileptiform discharges and its possible role in sustaining seizure-like events in neocortical slices. J. Neurophysiol. 92, 862–872. [PubMed: 15277598]

Shi Y, Abe C, Holloway BB, Shu S, Kumar NN, Weaver JL, Sen J, Perez-Reyes E, Stornetta RL, Guyenet PG, and Bayliss DA (2016). Nalcn is a “leak” sodium channel that regulates excitability of brainstem chemosensory neurons and breathing. J. Neurosci. 36, 8174–8187. [PubMed: 27488637]

Shi Y, Stornetta RL, Stornetta DS, Onengut-Gumuscu S, Farber EA, Turner SD, Guyenet PG, and Bayliss DA (2017). Neuromedin B expression defines the mouse retrotrapezoid nucleus. J. Neurosci. 37, 11744–11757. [PubMed: 29066557]

Shpak G, Zylbertal A, Yarom Y, and Wagner S (2012). Calcium-activated sustained firing responses distinguish accessory from main olfactory bulb mitral cells. J. Neurosci. 32, 6251–6262. [PubMed: 22553031]

Simard C, Hof T, Keddache Z, Launay P, and Guinamard R (2013). The TRPM4 non-selective cation channel contributes to the mammalian atrial action potential. J. Mol. Cell. Cardiol. 59, 11–19. [PubMed: 23416167]

Sobrinho CR, Kuo FS, Barna BF, Moreira TS, and Mulkey DK (2016). Cholinergic control of ventral surface chemoreceptors involves Gq/inositol 1,4,5-trisphosphate-mediated inhibition of KCNQ channels. J. Physiol. 594, 407–419. [PubMed: 26572090]

Souza GMPR, Kanbar R, Stornetta DS, Abbott SBG, Stornetta RL, and Guyenet PG (2018). Breathing regulation and blood gas homeostasis after near complete lesions of the retrotrapezoid nucleus in adult rats. J. Physiol. 596, 2521–2545. [PubMed: 29667182]

Stornetta RL, Moreira TS, Takakura AC, Kang BJ, Chang DA, West GH, Brunet JF, Mulkey DK, Bayliss DA, and Guyenet PG (2006). Expression of Phox2b by brainstem neurons involved in chemosensory integration in the adult rat. J. Neurosci. 26, 10305–10314. [PubMed: 17021186]

Surmeier DJ (2007). Calcium, ageing, and neuronal vulnerability in Parkinson’s disease. Lancet Neurol. 6, 933–938. [PubMed: 17884683]

Teruyama R, Sakuraba M, Kurotaki H, and Armstrong WE (2011). Transient receptor potential channel m4 and m5 in magnocellular cells in rat supraoptic and paraventricular nuclei. J. Neuroendocrinol. 23, 1204–1213. [PubMed: 21848647]

Ting JT, Daigle TL, Chen Q, and Feng G (2014). Acute brain slice methods for adult and aging animals: application of targeted patch clamp analysis and optogenetics. Methods Mol. Biol. 1183, 221–242. [PubMed: 25023312]

Tsuruyama K, Hsiao CF, and Chandler SH (2013). Participation of a persistent sodium current and calcium-activated nonspecific cationic current to burst generation in trigeminal principal sensory neurons. J. Neurophysiol. 110, 1903–1914. [PubMed: 23883859]

Wang LY, and Augustine GJ (2015). Presynaptic nanodomains: a tale of two synapses. Front. Cell. Neurosci. 8, 455. [PubMed: 25674049]

Wang S, Benamer N, Zanella S, Kumar NN, Shi Y, Bévengut M, Penton D, Guyenet PG, Lesage F, Gestreau C, et al. (2013a). TASK-2 channels contribute to pH sensitivity of retrotrapezoid nucleus chemoreceptor neurons. J. Neurosci. 33, 16033–16044. [PubMed: 24107938]

Wang S, Shi Y, Shu S, Guyenet PG, and Bayliss DA (2013b). Phox2bexpressing retrotrapezoid neurons are intrinsically responsive to H+ and CO2. J. Neurosci. 33, 7756–7761. [PubMed: 23637167]

Wu LJ, Sweet TB, and Clapham DE (2010). International Union of Basic and Clinical Pharmacology. LXXVI. Current progress in the mammalian TRP ion channel family. Pharmacol. Rev. 62, 381–404. [PubMed: 20716668]

Wu Y, Proch KL, Teran FA, Lechtenberg RJ, Kothari H, and Richerson GB (2019). Chemosensitivity of Phox2b-expressing retrotrapezoid neurons is mediated in part by input from 5-HT neurons. J. Physiol. 597, 2741–2766. [PubMed: 30866045]

Yu H, Xu K, Zou B, Wu M, McManus OB, Le Engers J, Cheung YY, Salovich JM, Hopkins CR, Lindsley CW, and Li M (2010). Identification of a novel, small molecule inhibitor of KCNQ2 channels. Probe Reports from the NIH Molecular Libraries Program (National Center for Biotechnology Information).

Yung WH, Häusser MA, and Jack JJ (1991). Electrophysiology of dopaminergic and non-dopaminergic neurones of the guinea-pig substantia nigra pars compacta in vitro. J. Physiol. 436, 643–667. [PubMed: 2061849]

Zhu ZT, Munhall A, Shen KZ, and Johnson SW (2004). Calcium-dependent subthreshold oscillations determine bursting activity induced by N-methyl-D-aspartate in rat subthalamic neurons in vitro. Eur. J. Neurosci. 19, 1296–1304. [PubMed: 15016087]

Highlights

- RTN respiratory neurons display large subthreshold membrane potential oscillations
- Voltage-dependent oscillations require TRPM4, a calcium-dependent cationic channel
- TRPM4-dependent oscillations support basal, pH-, and neuromodulator-evoked RTN firing
- TRPM4 contributes to tonic RTN-driven central respiratory output *in vivo*

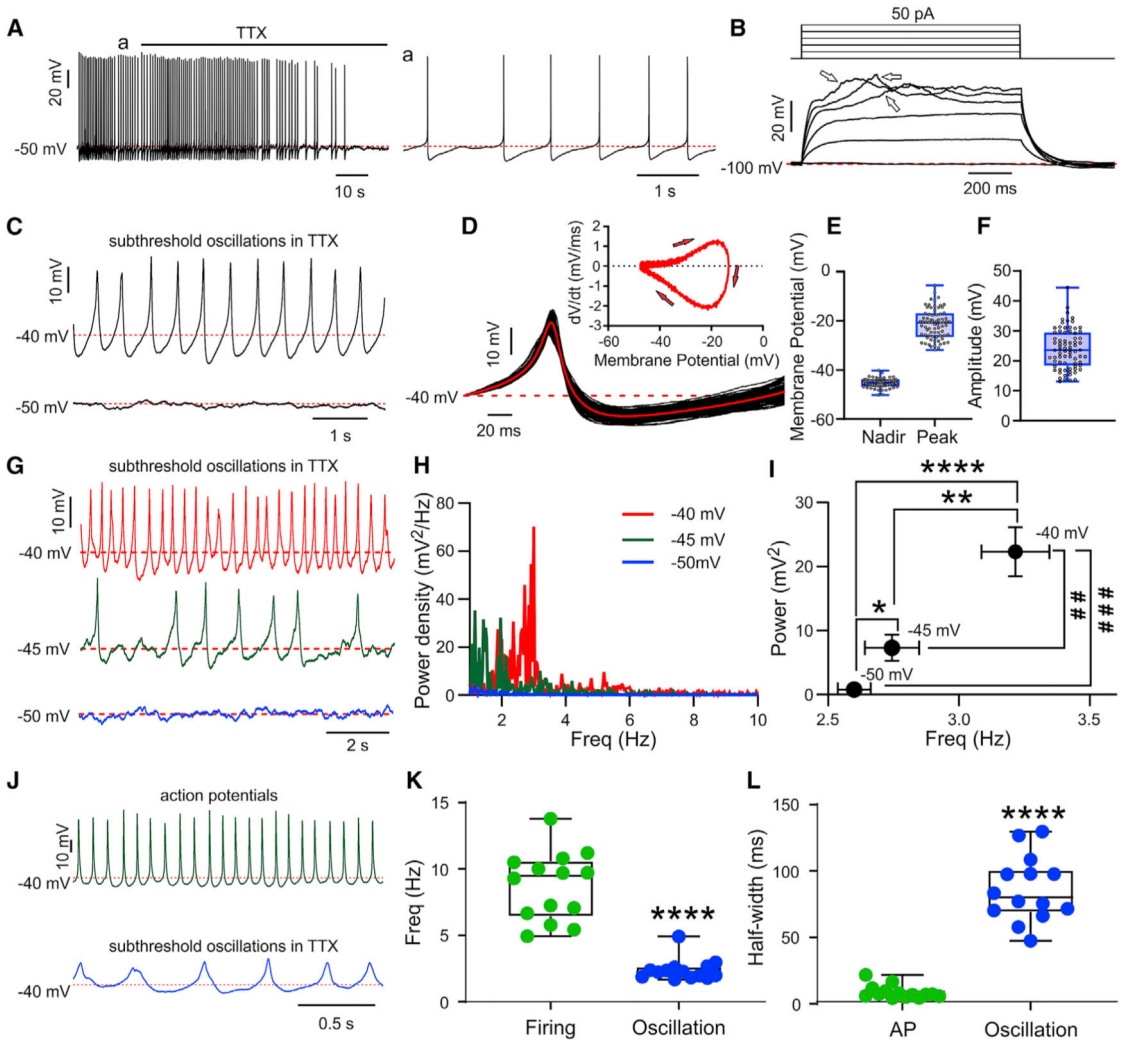

Figure 1. The properties of subthreshold oscillation in RTN neurons

(A) Spontaneous action potentials recorded in RTN neurons under whole-cell current clamp were abolished by TTX (0.5 μM); traces shown on expanded timescale. In this and all subsequent experiments, the bath solution contained fast synaptic blockers (10 μM CNQX, 10 μM bicuculline, and 30 μM strychnine).

(B) After TTX, depolarizing current injection (10 pA steps, from −100 mV) failed to elicit action potentials; active depolarizing potentials were superimposed on the passive response with larger current pulses (arrows).

(C) In TTX, small membrane potential fluctuations at −50 mV were transformed into large subthreshold oscillations when DC was injected (to ~−40 mV).

(D) Individual oscillations for a period of 30 s at −40 mV are overlaid (black) and averaged (red). Inset: Phase-plane plot of the averaged oscillation waveform. (A–D from the same neuron).

(E and F) The nadir and peak (E) and amplitude (F) of averaged subthreshold oscillation waveforms (n = 75).

(G and H) Subthreshold oscillations were obtained at the indicated membrane potentials by DC injection (G), and corresponding power density-frequency plots were determined by FFT (H).

(I) Integrated power and mean frequency of subthreshold oscillations (mean ± SEM) recorded at three membrane potentials in the same neurons. $F_{2,36} = 24$, $p < 0.0001$ for power; $F_{2,36} = 13.83$, $p < 0.0001$ for frequency by repeated measures (RM) ANOVA with Tukey's post hoc test; *p = 0.011, **p = 0.001, ****p < 0.0001; ##p = 0.003, ###p = 0.0008; n = 19.

(J) Action potentials and subthreshold oscillations recorded in the same neuron at −40 mV (by DC injection).

(K and L) Summary data of frequency (K) and duration (half-width) (L) for spontaneous firing and subthreshold oscillations. By paired t test: ****p < 0.0001; n = 14. Box and whiskers plots in this and other figures show a box bounded by the 25th and 75th percentiles and bisected by the median, with whiskers defining the range. Source data for all figure panels is provided in Data S1.

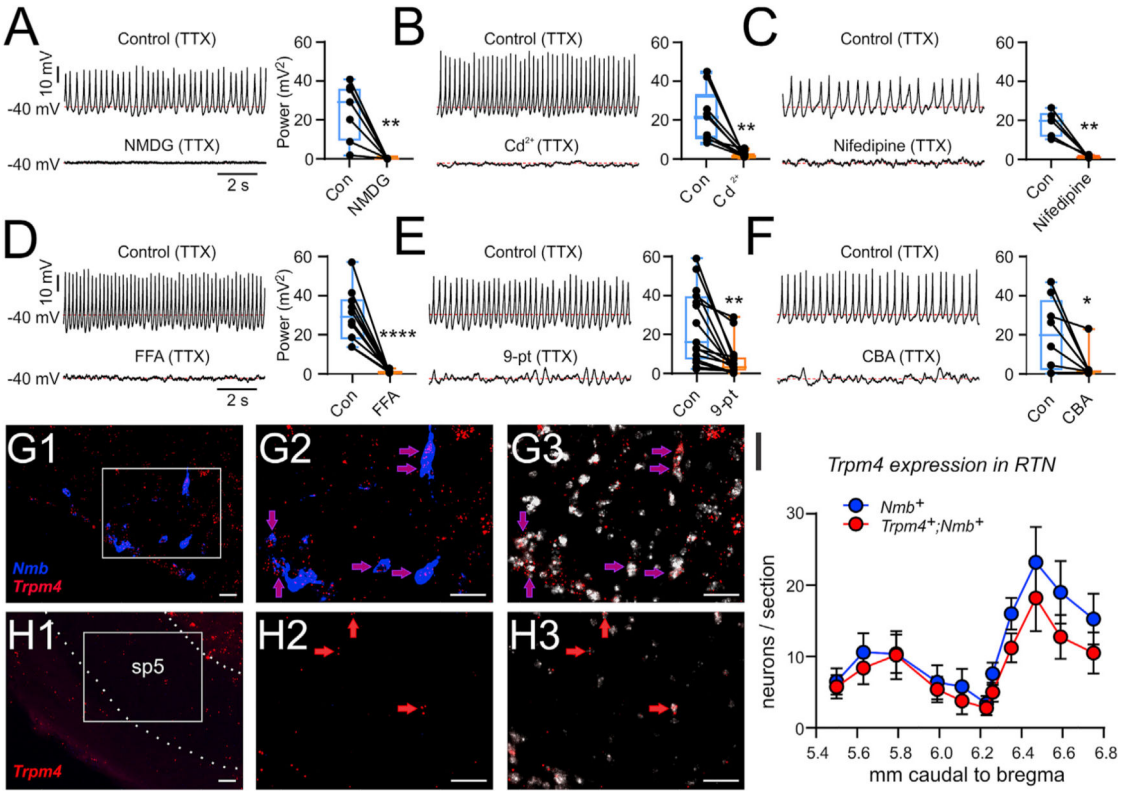

Figure 2. Ca^{2+}- and Na^{+}-dependent subthreshold oscillations involve TRPM4 channels in RTN neurons

(A–F) Effects on subthreshold oscillations in TTX (0.5 μM TTX, at −40 mV with DC injection) of bath application of NMDG (A), substituted for Na^{+}; Cd^{2+} (B), (100 μM); nifedipine (C), L-type Ca^{2+} channel blocker (at 10 μM); flufenamate (D), broad-spectrum TRP channel blocker (at 100 μM); and two TRPM4 channel blockers, 9-phenanthrol (E) (30 μM) and CBA (F) (50 μM). Summary data depict effects of each manipulation on integrated power (from FFT analysis) for all cells. Statistical analyses by paired t test: NMDG ($p = 0.005$, $n = 7$); Cd^{2+} ($p = 0.003$, $n = 9$); nifedipine ($p = 0.007$, $n = 5$); FFA ($p < 0.0001$, $n = 10$); 9-pt ($p = 0.002$, $n = 15$); CBA ($p = 0.036$, $n = 8$). Box and whiskers plots as in Figure 1.

(G and H) RNA-scope analysis of *Nmb* (blue) and *Trpm4* (red) transcript expression in the RTN (G) and the spinal trigeminal tract (H; sp5). The boxed regions are shown at higher power (G2 and H2) and with *Trpm4* labeling overlaid on DAPI nuclei stain (G3 and H3). Scale bars, 50 μm.

(I) Rostrocaudal distribution of *Trpm4*-expressing cells (mean ± SEM) within the population of *Nmb*-expressing RTN neurons (n = 5, adult mice).

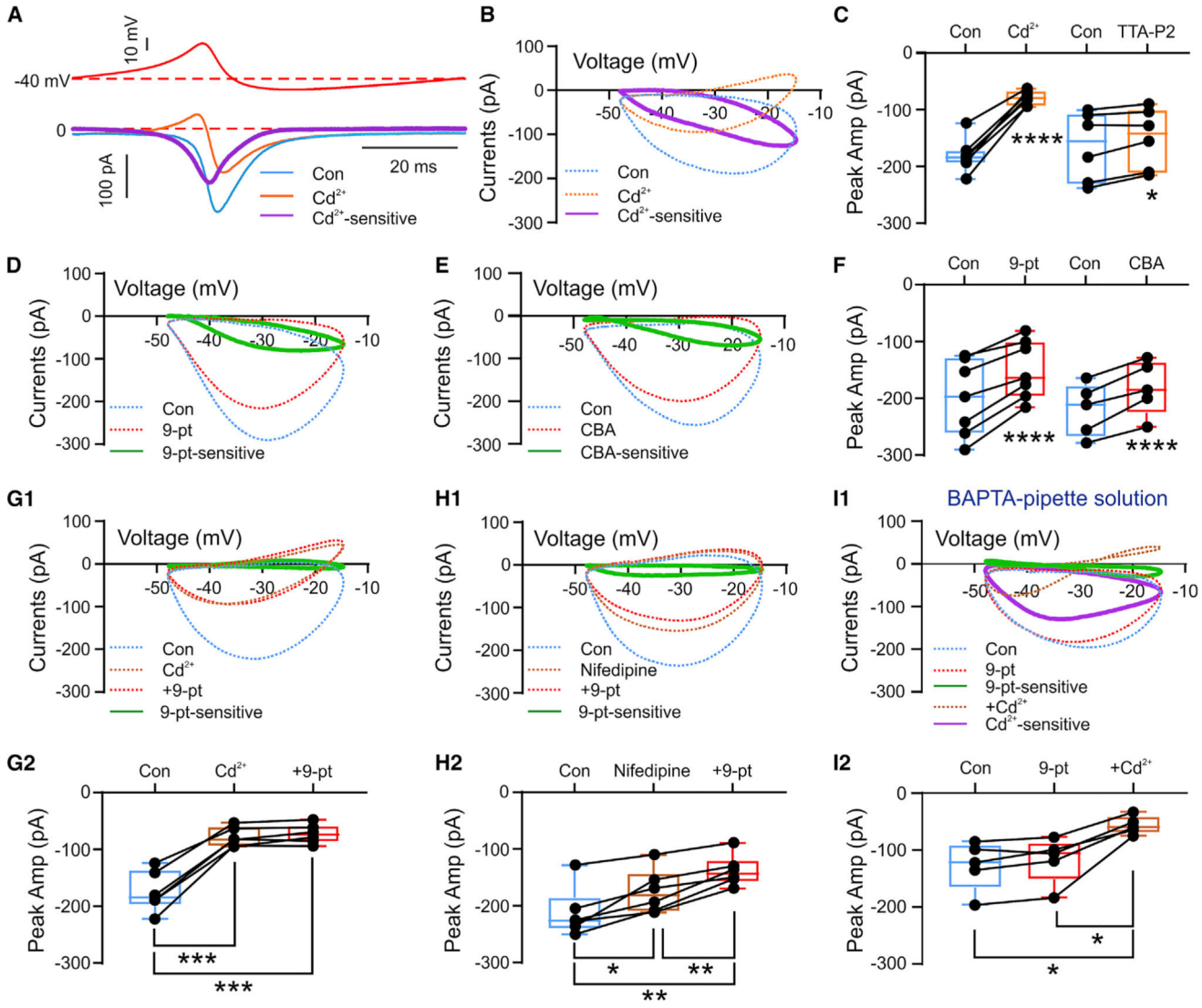

Figure 3. Calcium-dependent TRPM4 currents contribute to subthreshold oscillations in RTN neurons

(A) Top, Oscillation-waveform voltage command applied from Vhold = −40 mV. Bottom, Oscillation-waveform-evoked currents in cells recorded with a Cs^+-based pipette solution under control conditions and in the presence of 200 μM Cd^{2+} were subtracted to obtain the Cd^{2+}-sensitive current (purple).

(B) *I*-V curves of oscillation-waveform-induced currents reveal inward Cd^{2+}-sensitive current throughout the oscillation waveform.

(C) Effects on peak oscillation-waveform-evoked currents of Cd^{2+} ($p < 0.0001$, n = 7) and TTA-P2 (1 uM, $p = 0.025$, n = 6), both by paired t test. Box and whiskers plots in all panels as in Figure 1.

(D and E) *I*-V curves of oscillation-waveform-induced currents before and during exposure to 9-pt (30 μM) (D) or CBA (50 μM) (E).

(F) Effects of TRPM4 blockers on peak oscillation-waveform-evoked currents (9-pt, $p = 0.0004$, n = 7; CBA, $p = 0.0025$, n = 5, by paired t test.).

(G and H) The *I*-V curves of 9-pt-sensitive oscillation-waveform-evoked current were eliminated after blocking calcium currents with Cd^{2+} (200 μM; G1) or strongly inhibited by inhibiting L-type channels with nifedipine (10 μM; H1). This finding is reflected in summary data of peak oscillation-waveform-evoked currents under those conditions (G2: $F_{2,10} = 110.9$, $p < 0.0001$; control versus Cd^{2+}, $p = 0.0003$; control versus Cd^{2+}+9-pt, $p = 0.0002$; Cd^{2+} versus Cd^{2+}+9-pt, $p = 0.3$, $n = 6$; H2: $F_{2,10} = 30.83$, $p = 0.0002$; control versus nifedipine, $p = 0.03$; control versus nifedipine+9-pt, $p = 0.003$; nifedipine versus nifedipine +9-pt, $p = 0.008$, $n = 6$; both by RM ANOVA with Tukey's post hoc test).

(I1) *I*-V curves of oscillation-waveform-induced currents in cells recorded with pipettes containing 10 mM BAPTA to chelate intracellular Ca^{2+} (pCa, ~8).

(I2) Peak oscillation-waveform-evoked currents in BAPTA-containing cells were unaffected by 9-pt (30 μM) but inhibited by subsequent application of Cd^{2+} (100 μM); $F_{2,8} = 23.45$, $p = 0.0043$; control versus 9-pt, $p = 0.22$; 9-pt versus 9-pt+Cd^{2+}, $p = 0.02$; control versus Cd^{2+}, $p = 0.01$, $n = 5$, by RM ANOVA with Tukey's post hoc test.

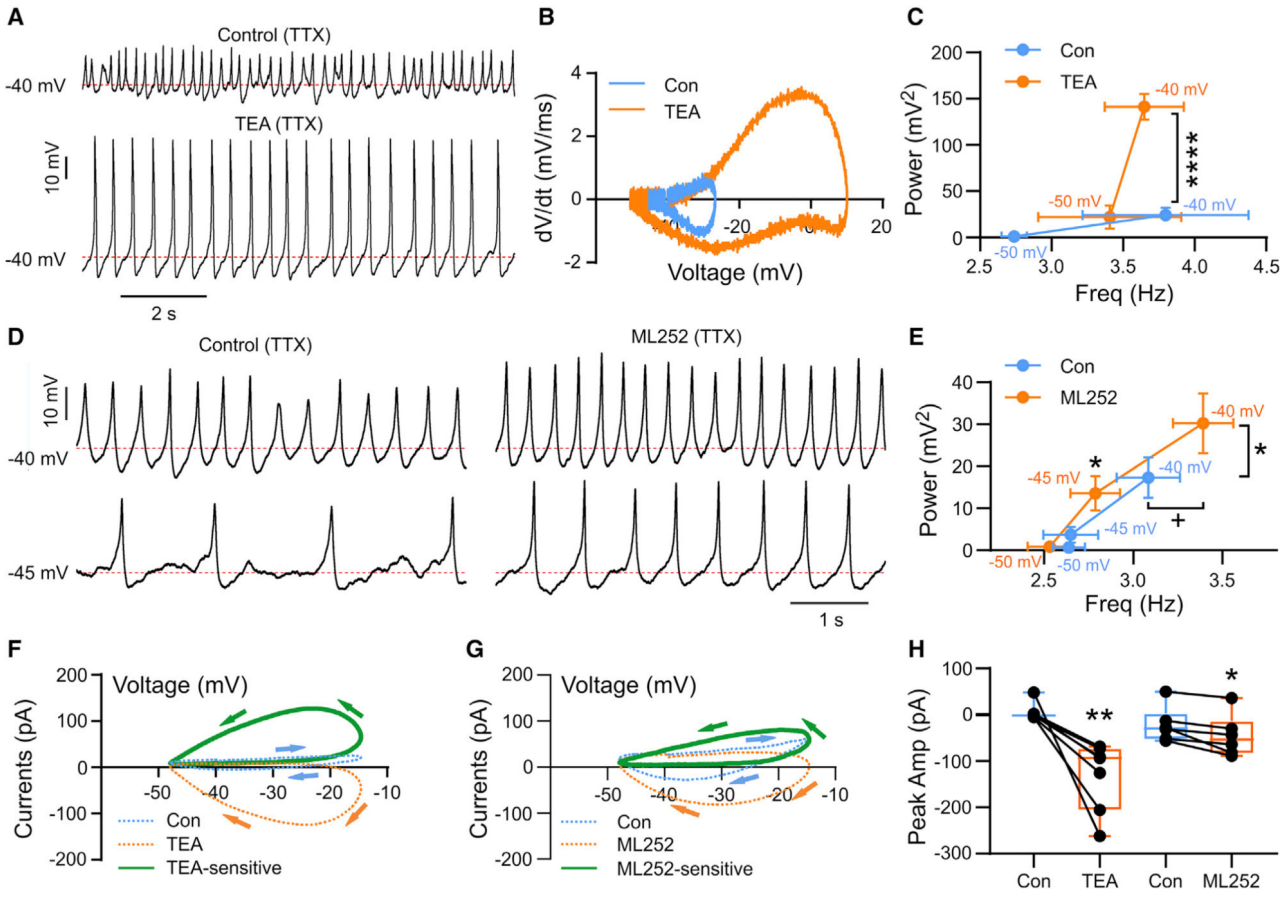

Figure 4. Voltage-activated K^+ channels constrain the subthreshold oscillation in RTN neurons

(A) Subthreshold oscillations (0.5 μM TTX, at −40 mV with DC injection), before and after TEA (10 mM).

(B) Phase-plane plot of averaged oscillation in control (blue) and TEA (orange).

(C), Integrated power and mean frequency of subthreshold oscillations before and after TEA (mean ± SEM, n = 7). RM ANOVA with Sidak's post hoc: $F_{1,6} = 35.11$, $p < 0.001$ for TEA effect on power, ****$p < 0.0001$; $F_{1,6} = 0.5135$, $p = 0.5006$ for TEA effect on frequency.

(D) Subthreshold oscillations (0.5 μM TTX, at −45 mV and −40 mV with DC injection) under control conditions and in the presence of the KCNQ channel inhibitor ML252 (10 μM).

(E) Effect of ML252 on integrated power and mean frequency of subthreshold oscillations at the indicated membrane potentials (mean ± SEM, n = 9). RM ANOVA with Sidak's post hoc: $F_{1,8} = 17.08$, $p = 0.0033$ for ML252 effect on power, *$p < 0.05$; $F_{2,16} = 4.265$, $p = 0.0328$, for frequency x membrane potential test; +, $p = 0.0231$.

(F and G) *I*-V plots of oscillation-waveform-induced currents in cells recorded with a K^+-based pipette solution reveal outward currents sensitive to TEA (F) and ML252 (G).

(H) TEA and ML252 significantly increased peak oscillation-waveform-evoked inward current (control versus TEA: $p = 0.007$, n = 7; control versus ML252: $p = 0.02$, n = 6; by paired t test). Box and whiskers plots as in Figure 1.

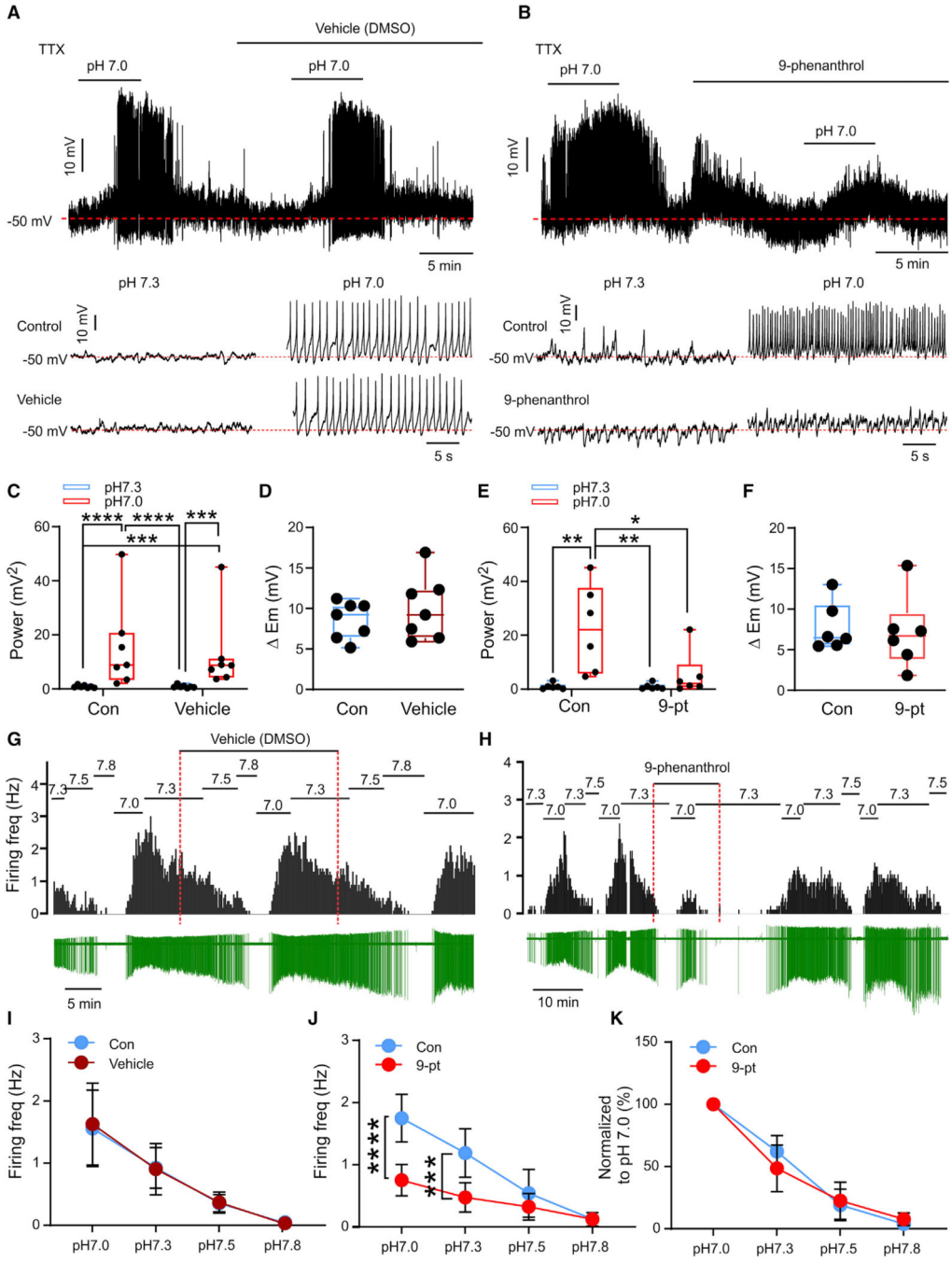

Figure 5. Acidosis-induced membrane potential depolarization activates TRPM4-dependent subthreshold oscillations in RTN neurons

(A and B) Effect on subthreshold oscillations (in TTX, 0.5 μM) of repeated exposures to acidified bath under control conditions and then during bath application of vehicle (DMSO; A) or 9-pt (30 μM; B). The cells were initially set at −50 mV using DC injection, which remained fixed throughout the experiment.

(C and E) Integrated power of membrane oscillations in RTN neurons under control conditions and then either in vehicle (C; n = 7) or in 9-pt (E; n = 6). RM ANOVA with Tukey's post hoc test: for vehicle, $F_{1,6} = 2.186$, p = 0.19; for 9-pt, $F_{1,5} = 14.4$, p = 0.013; *p

< 0.05, **p < 0.01, ***p < 0.001, ****p < 0.0001. Box and whiskers plots in all panels as in Figure 1.

(D and F) Acidosis-evoked membrane depolarization under control conditions and then either in vehicle (D; p = 0.27; n = 7) or in 9-pt (F; p = 0.5; n = 6), by paired t test.

(G and H) Representative rate histograms (top) and cell-attached recordings (bottom) of spontaneous firing responses of RTN neurons during changes of bath pH before and after exposure to vehicle (DMSO; G) or 9-pt (H). Recordings in the presence of synaptic blockers, but no TTX.

(I and J) Effect of changes in pH on firing frequency (mean ± SEM) under control conditions and after exposure to vehicle (I; n = 5) or 9-pt (J; n = 8). RM ANOVA with Tukey's post hoc test: For vehicle, $F_{1,4} = 0.043$, p = 0.85; for 9-pt, $F_{1,7} = 14.1$, p = 0.007, ***p < 0.001, ****p < 0.0001.

(K) Firing frequencies in control and 9-pt (from J) were normalized to peak frequency and plotted relative to bath pH (mean ± SEM).

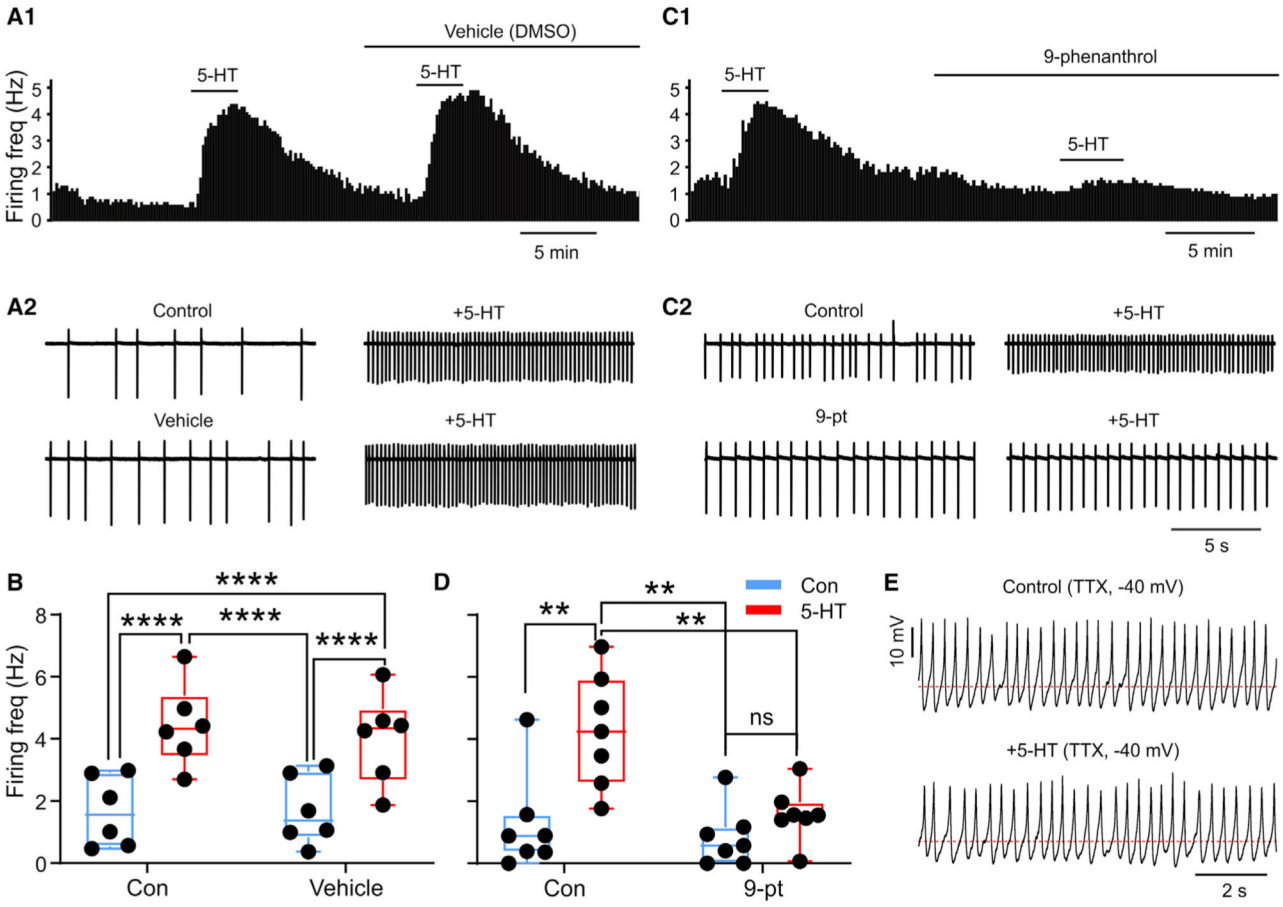

Figure 6. TRPM4 supports activation of RTN neurons by 5-HT

(A–C) Firing rate histograms of RTN neuron firing rate (cell-attached recordings) under control conditions and in the presence of 5-HT (10 μM) before and after exposure to either vehicle (DMSO; A) or 9-pt (C). Recordings in the presence of synaptic blockers, but no TTX.

(B and D) Firing frequency response to 5-HT under control conditions and after exposure to vehicle (C; n = 6) or 9-pt (D; n = 7). RM ANOVA with Tukey's post hoc test: For vehicle, $F_{1,5} = 2.57$, $p = 0.17$; for 9-pt, $F_{1,6} = 45.95$, $p = 0.0005$; **$p < 0.01$, ****$p < 0.0001$. Box and whiskers plots as in Figure 1.

(E) Representative traces of subthreshold oscillation before and during 5-HT (in TTX, at −40 mV with DC injection).

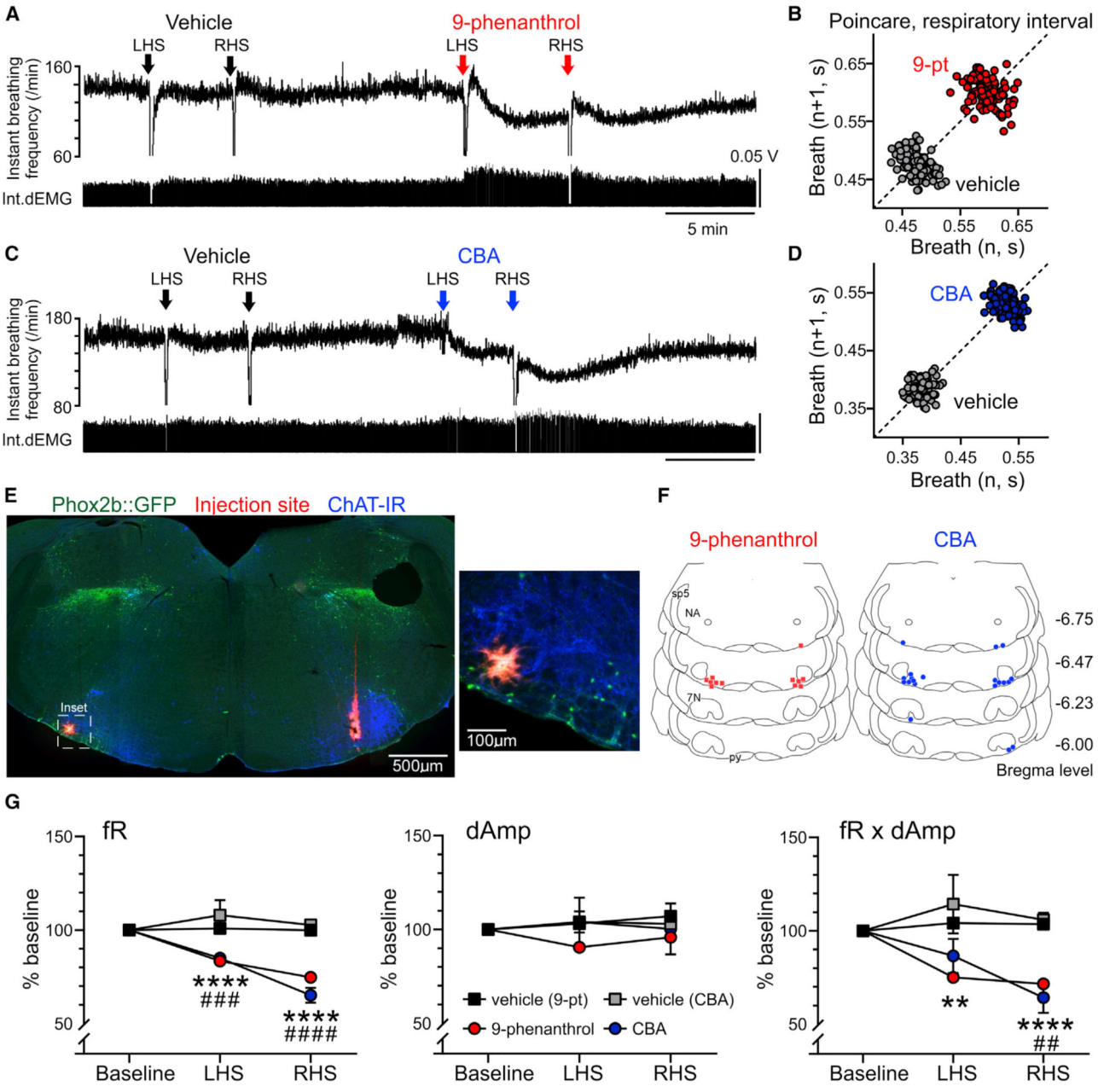

Figure 7. TRPM4 inhibition in RTN reduces respiratory output in mice

(A and C) Effect on diaphragm EMG (dEMG) of bilateral injections (30–40 nL) of vehicle and 9-pt (A; 30 µM) or CBA (C; 50 µM) in the RTN of freely breathing, anesthetized adult Phox2b::GFP mice. LHS, left hand side; RHS, right hand side.

(B and D) Poincaré analysis of breath-to-breath frequency after vehicle, 9-pt (B), and CBA (D) from the corresponding experiments (in A and C).

(E) Transverse brainstem section showing location of bilateral injection sites (marked by red fluorescent latex beads) in the RTN; expanded image shows the close proximity of the left injection site to GFP^{+} RTN neurons. ChAT, choline acetyltransferase.

(F) Distribution of RTN injection sites of 9-pt (n = 6) and CBA (n = 10).

(G) Grouped data (mean ± SEM) for on-target bilateral injections of vehicle, 9-pt, or CBA in the RTN. For fR and fR × dAmp, there was a significant interaction between injection number and drug for both 9-pt and CBA, relative to vehicle. 9-pt versus vehicle: fR, $F_{2,39}$ = 30.43, $p < 0.0001$; fR × dAmp, $F_{2,39}$ = 6.417, $p = 0.0039$. CBA versus vehicle: fR, $F_{2,42}$ = 13.63, $p < 0.0001$; fR × dAmp, $F_{2,42}$ = 3.299, $p = 0.0467$. **/$^{\#\#}p < 0.01$, ***/$^{\#\#\#}p < 0.001$, ****/$^{\#\#\#\#}p < 0.0001$, for 9-phenanthrol/CBA versus vehicle by Sidak's multiple comparison test.

KEY RESOURCES TABLE

REAGENT or RESOURCE	SOURCE	IDENTIFIER
Antibodies		
Chicken anti-GFP	Aves Labs, Davis, CA, Cat # GFP-1020	RRID: AB_10000240
Alexa Fluor 488 AffiniPure Donkey Anti-Chicken	Jackson Immunoresearch, West Grove, PA, Cat # 703-545-155	RRID:AB_2340375
Goat anti-Chat	Millipore-Sigma, Cat # AB144P	RRID:AB_2079751
Alexa Fluor 647 AffiniPure Donkey Anti-Goat	Jackson Immunoresearch, West Grove, PA, Cat # 705-605-147	RRID: AB_2340437
Chemicals, peptides, and recombinant proteins		
Tetrodotoxin	TOCRIS	Cat# 1078
9-phenanthrol	TOCRIS	Cat # 4999
CBA	TOCRIS	Cat # 6724
Flufenamic acid	Sigma-Aldrich	Cat # F9005; CAS:530-78-9
Nifedipine	Sigma-Aldrich	Cat # N7634; CAS:21829-25-4
TTA-P2	Alomone labs	Cat # T-155; CAS:918430-49-6, 1072018-68-8
ω-conotoxin GVIA	Alomone labs	Cat#C-300; CAS:106375-28-4
ω-Agatoxin IVA	Alomone labs	Cat#STA-500; CAS:145017-83-0
TC-N1752	TOCRIS	Cat # 4435
Tetraethylammonium chloride	Sigma-Aldrich	Cat # T2265; CAS:56-34-8
ML252	Sigma-Aldrich	Cat # SML0723; CAS:1392494-64-2
Serotonin hydrochloride	Sigma-Aldrich	Cat # H9523; CAS:153-98-0
CNQX	Sigma-Aldrich	Cat # C127; CAS:115066-14-3
Bicuculline	Sigma-Aldrich	Cat # 14340; CAS:485-49-4
Strychnine	Sigma-Aldrich	Cat # S8753; CAS:1421-86-9
1,2-Bis(2-aminophenoxy)ethane-*N,N,N′,N′*-tetraacetic acid	Sigma-Aldrich	Cat # A4926; CAS:85233-19-8
N-Methyl-D-glucamine	Sigma-Aldrich	Cat # M2004; CAS:6284-40-8
Critical commercial assays		
RNAscope® Multiplex Fluorescent Reagent Kit V2	Advanced Cell Diagnostics (ACD)	Cat#323100; RRID:SCR_012481
Deposited data		
RTN neuron single cell RNA-Seq data	Shi et al., 2017; PMID: 29066557	GEO Accession# GSE163155
Experimental models: organisms/strains		
Mouse: Phox2b::GFP BAC transgenic mouse line (Jx99)	Lazarenko et al., 2009; PMID: 19711410	N/A
Oligonucleotides		

REAGENT or RESOURCE	SOURCE	IDENTIFIER
Probe for NMB, target region:14 – 685 (Accession # NM_001291280.1)	Advanced Cell Diagnostics (ACD)	Cat No. 459931-C2
Probe for Trpm4, target region: 1289 – 2224 (Accession # NM_175130.4)	Advanced Cell Diagnostics (ACD)	Cat # 534621
Software and algorithms		
pCLAMP Clampex Software (9.2)	Molecular Devices	RRID:SCR_011323
GraphPad Prism 8.1.1	GraphPad	RRID:SCR_002798
MATLAB R2019b	MathWorks	N/A
Neurolucida	MBF Bioscience	RRID:SCR_001775
CorelDRAW X7	COREL	RRID:SCR_014235
Spike2 (V.8.0)	Cambridge Electronic Design	RRID:SCR_000903